

A BROADBAND X-RAY STUDY OF A SAMPLE OF AGNs WITH [OIII] MEASURED INCLINATIONS

X. ZHAO¹, S. MARCHESI^{1,2}, M. AJELLO¹, M. BALOKOVIĆ^{3,4}, T. FISCHER⁵

Draft version April 8, 2020

ABSTRACT

In modeling the X-ray spectra of active galactic nuclei (AGNs), the inclination angle is a parameter that can play an important role in analyzing the X-ray spectra of AGN, but it has never been studied in detail. We present a broadband X-ray spectral analysis of the joint *NuSTAR*-XMM-*Newton* observations of 13 sources with [OIII] measured inclinations determined by Fischer et al. (2013). By freezing the inclination angles at the [OIII] measured values when modeling the observations, the spectra are well fitted and the geometrical properties of the obscuring structure of the AGNs are slightly better constrained than those fitted when the inclination angles are left free to vary. We also test if one could freeze the inclinations at other specific angles in fitting the AGN X-ray spectra as commonly did in the literatures. We find that one should always let the inclination angle free to vary in modeling the X-ray spectra of AGNs, while fixing the inclination angle at [OIII] measured values and fixing the inclination angle at 60° also present correct fits of the sources in our sample. Correlations between the covering factor and the average column density of the obscuring torus with respect to the Eddington ratio are also measured, suggesting that the distribution of the material in the obscuring torus is regulated by the Eddington ratio, which is in agreement with previous studies. In addition, no geometrical correlation is found between the narrow line region of the AGN and the obscuring torus, suggesting that the geometry might be more complex than what is assumed in the simplistic unified model.

Keywords: galaxies: active – galaxies: nuclei – galaxies: individual (Mrk 3, Mrk 34, Mrk 78, Mrk 573, Mrk 1066, NGC 3227, NGC 3783, NGC 4051, NGC 4151, NGC 4507, NGC 5506, NGC 5643, NGC 7674) – X-rays: galaxies

1. INTRODUCTION

It is commonly accepted that the main structure of an active galactic nucleus (AGN) is composed of a supermassive black hole (SMBH; $M_{\text{BH}} \approx 10^{6-9.5} M_{\odot}$) at the center of the AGN, an accretion disk surrounding the SMBH, a subparsec-scale dust-free region known as the broad line region (BLR), where broad lines with full-width at half-maximum (FWHM) $> 2000 \text{ km s}^{-1}$ are observed in optical, a parsec-scale toroidal structure composed of gas and dust obscuring the emission from the center engine of the AGN, and a broaden structure ($\sim 10 \text{ pc}$ to $\sim 1 \text{ kpc}$) namely the narrow line region (NLR; FWHM $< 1000 \text{ km s}^{-1}$; see, e.g., Netzer 2015; Almeida & Ricci 2017; Hickox & Alexander 2018, for recent reviews). AGNs are optically classified as type 1 or type 2 AGNs, if the broad-emission lines can be observed in their optical spectra or not. According to the AGN unified model (Antonucci 1993; Urry & Padovani 1995), type 2 AGNs are the AGNs whose line-of-sight between the central engine and the observer passes the dusty toroidal structure and type 1 AGNs are those whose line-of-sight does not intercept the torus. Furthermore, the torus is also thought to

play an important role in the co-evolution of the SMBH and the host galaxy (see, e.g., Kormendy & Ho 2013; Heckman & Best 2014). Therefore, putting strong constraints on the physical and geometrical properties of the toroidal structure is essential to understand the basics of AGNs.

Observing the X-ray emission from AGNs is a powerful method to probe their obscuring toroidal structure. The intrinsic X-ray emission produced by the central engine of the AGN is reprocessed by the obscuring torus: studying this reprocessed X-ray emission can then provide abundant of information about the properties of the torus. One of the ubiquitous signatures of this reprocessed component is the fluorescent Fe K α line at 6.4 keV, originating from the outer side of the accretion disk or the inner edge of the torus (see, e.g., Fabian et al. 2000; Reynolds & Nowak 2003; Yaqoob & Padmanabhan 2004, for reviews), which could provide significant information on both the physics and dynamics of the circumnuclear materials (Leahy & Creighton 1993; Reynolds 1999; Matt 2002; Shu et al. 2010; Ricci et al. 2014). XMM-*Newton* is the best instrument to study such a signature in terms of both effective area between 0.3 keV to 10 keV and spectral resolution. Indeed, many studies have been done on the properties of the torus utilizing XMM-*Newton* (e.g., Georgantopoulos et al. 2013; LaMassa et al. 2014). Another spectral signature of the reprocessed component, which is particularly prominent in heavily obscured AGN (i.e., sources with column density $N_{\text{H}} \geq 10^{24} \text{ cm}^{-2}$), is the so called “Compton hump” peaked at 10–40 keV (see, e.g., Ghisellini et al. 1994; Krolik et al. 1994). Thus the proper characterization of heavily obscured AGNs, which

¹ Department of Physics & Astronomy, Clemson University, Clemson, SC 29634, USA

² INAF-Osservatorio Astronomico di Bologna, Via Piero Gobetti, 93/3, I-40129, Bologna, Italy

³ Center for Astrophysics | Harvard & Smithsonian, 60 Garden Street, Cambridge, MA 02138, USA

⁴ Black Hole Initiative at Harvard University, 20 Garden Street, Cambridge, MA 02138, USA

⁵ Astrometry Department, United States Naval Observatory, 3450 Massachusetts Ave., NW, Washington, DC 20392, USA

are thought to be $\sim 20\text{-}30\%$ of all AGNs according to different CXB synthesis models predictions (Alexander et al. 2003; Gandhi & Fabian 2003; Gilli et al. 2007; Treister et al. 2009; Ueda et al. 2014; Ananna et al. 2019), requires an X-ray telescope sensitive above 10 keV. The launch of the *Nuclear Spectroscopic Telescope Array* (hereafter, *NuSTAR*, Harrison et al. 2013), which is the first instrument to focus on X-ray at energy >10 keV and provides a two orders of magnitude better sensitivity than previous telescopes (e.g., *INTEGRAL* and *Swift*-BAT; Winkler et al. 2003; Barthelmy et al. 2005) at $\sim 10\text{-}50$ keV, allowed us to characterize the physical properties of heavily obscured AGNs with unprecedented accuracy (e.g., Baloković et al. 2014; Puccetti et al. 2014; Annuar et al. 2015; Ursini et al. 2015; Koss et al. 2016; Marchesi et al. 2017; Ursini et al. 2018). Therefore, the combination of *NuSTAR* and *XMM-Newton* is one of the best methods to study the properties of an heterogeneous AGN population in the local universe (see, e.g., Marinucci et al. 2014; Fürst et al. 2016; Ursini et al. 2016; La Caria et al. 2019; Marchesi et al. 2019; Walton et al. 2019; Zhao et al. 2019a,b).

In recent years, several tori models based on Monte Carlo simulation have been developed to characterize the X-ray spectra of AGNs (Matt & Fabian 1994; Ikeda et al. 2009; Murphy & Yaqoob 2009; Brightman & Nandra 2011; Paltani, S. & Ricci, C. 2017; Baloković et al. 2018; Tanimoto et al. 2019). Different models adopt different assumptions on the geometry of the torus, e.g., Murphy & Yaqoob (2009); Liu & Li (2014); Furui et al. (2016) assume a half-opening angle of the torus fixed at $\theta_{\text{h.o.}} = 60^\circ$ but variable inclination angle of the torus (θ_{obs}); Ikeda et al. (2009); Brightman & Nandra (2011); Paltani, S. & Ricci, C. (2017); Baloković et al. (2018); Tanimoto et al. (2019) assume a flexible half-opening angle of the torus and variable inclination angle. Given the intrinsic complexity of these models and the multiple free parameters involved, applying them in full capability is still difficult especially with low-quality X-ray spectra: in particular, the inclination angle of the AGN is hard to constrain. Thus it is common to freeze θ_{obs} in the spectral analysis process (see, e.g., Yaqoob 2012; Kawamuro et al. 2013; Brightman et al. 2015; Yaqoob et al. 2015; Koss et al. 2015, 2016; Ricci et al. 2016; Gandhi et al. 2017; Marchesi et al. 2018). However, the validity of the method of freezing the inclination angle has not yet been studied in a systematic way. The studies on the NLRs of AGNs can provide us with a method to overcome this issue by measuring the inclinations of the AGNs by mapping the kinematics of their NLRs. Fischer et al. (2013) successfully measured the inclinations of the NLRs and thus the torus with respect to our line-of-sight in 17 AGNs by fitting the radial outflow dominated NLR kinematics resolved by *Hubble Space Telescope* (HST) [OIII] imaging and Space Telescope Imaging Spectrograph (STIS) with a biconical outflow model.

In this work, we study the role of inclination angle in fitting the AGN X-ray spectra by comparing the best-fit results obtained when the broad X-ray spectra of the sources in the sample of Fischer et al. (2013) are fitted with the inclination angle being (i) left free to vary, (ii) fixed at [OIII] measured values, (iii) fixed at 60° and (iv) fixed at 87° . The paper is organized as follows: in Section 2, we report the sample selection rules and the *NuSTAR*,

XMM-Newton and *Chandra* data reduction process; in Section 3, we describe the model used to fit the broadband X-ray spectra, the fitting procedure and best-fit results of each source in our sample; in Section 4, we discuss how fixing the inclination angle affects the broadband X-ray spectral analysis of AGNs and study the geometrical properties of the AGNs in both X-ray and optical. All reported uncertainties on spectral parameters are at 90% confidence level. Standard cosmological parameters are adopted as follows: $\langle H_0 \rangle = 70 \text{ km s}^{-1} \text{ Mpc}^{-1}$, $\langle q_0 \rangle = 0.0$ and $\langle \Omega_\Lambda \rangle = 0.73$.

2. SAMPLE SELECTION AND DATA REDUCTION

2.1. Selection Rule

To better constrain and properly study the physical and geometrical properties of AGNs, we utilize the sample reported in Fischer et al. (2013), who measured the nuclear inclinations of 17 nearby AGNs ($z < 0.1$) in optical. In these 17 AGNs, 15 sources have high-quality *NuSTAR* archival data (the 2 sources without *NuSTAR* archival data are Mrk 279 and NGC 1667). All 15 sources also have *XMM-Newton* archival observations: for 6 of these 15 sources, the *NuSTAR* and *XMM-Newton* observations were taken simultaneously. We also supplement *Chandra* data for three sources, i.e., Mrk 34, Mrk 78 and Mrk 1066, of which the *XMM-Newton* spectra is not in high-quality. The summary of the observations is reported in Table 1.

It is worth mentioning that 2 sources in the Fischer et al. (2013) sample are excluded in our analysis, which are Circinus and NGC 1068. The Circinus AGN X-ray spectra has been shown to be contaminated by two bright off-nuclear X-ray sources, the X-ray binary CGX1 and the supernova remnant CGX2 (Bauer et al. 2001). Furthermore, Arévalo et al. (2014) showed that the contamination from CGX1 and CGX2 contributes to 18% of the nuclear flux in the Iron line region and becomes comparable to the nuclear flux at energy >30 keV. The off-nuclear sources can be resolved by *XMM-Newton*, but not by *NuSTAR*. Therefore, Circinus is excluded from our sample due to the fact we do not have the ability to extract the AGN broadband X-ray spectrum of Circinus without any contamination. Furthermore, NGC 1068 is also excluded from our final sample, since we find that it is difficult to fit both *NuSTAR* and *XMM-Newton* spectra properly with the standard model presented in Section 3.1. Indeed, Bauer et al. (2015) suggests a best-fit model of three reprocessed components with distinct column densities, rather than the single reprocessed component used in our analysis. Therefore, 13 sources are analyzed as our finalized sample in the rest of the work.

2.2. Data Reduction

2.2.1. *NuSTAR*

For *NuSTAR* data, the raw files are calibrated, cleaned and screened using the *NuSTAR* `nupipeline` script version 0.4.6 and calibration database (CALDB) version 20181030. The sources spectra, ancillary response files (ARF) and response matrix files (RMF) are obtained using the `nuproducts` script version 0.3.0. The sources spectra are extracted from a $75''$ circular region, unless otherwise indicated, corresponding to $\approx 80\%$ of the encircled energy fraction (EEF) at 10 keV, centered on the

Table 1
Inclination angle of 15 sources in Fischer et al. (2013)

Source	z	$\log(M_{\text{BH}})^{\text{a}}$	$i_{\text{AGN}}^{\text{b}}$ (deg)	$\theta_{\text{max}}^{\text{c}}$ (deg)	<i>NuSTAR</i> date	<i>NuSTAR</i> ^d ks	XMM date	XMM ^e ks	<i>Chandra</i> date	<i>Chandra</i> ^f ks
Circinus	0.00145	6.23	65	41	2013 Jan 25	108	2013 Feb 03	131		
Mrk 3	0.01351	8.65	85	51	2015 Apr 08	50	2015 Apr 08	7		
Mrk 34	0.05050	7.12	65	40	2013 Sept 19	48	2005 Apr 04	31	2017 Jan 30	100
Mrk 78	0.03715	7.87	60	35	2018 Nov 19	48	2006 Mar 11	16	2017 Jan 01	50
...	2017 Jan 07	50
Mrk 573	0.01718	7.28	60	53	2018 Jan 06	64	2004 Jan 15	33		
Mrk 1066	0.01202	7.01	80	25	2014 Dec 06	60	2005 Feb 20	33	2003 July 14	20
NGC 1068	0.00379	7.20	85	40	2015 Feb 05	108	2015 Feb 03	89		
NGC 3227	0.00386	7.56	15	55	2016 Dec 01	84	2016 Dec 01	176		
NGC 3783	0.00973	6.94	15	55	2016 Dec 11	52	2016 Dec 11	126		
NGC 4051	0.00234	6.24	12	25	2013 Oct 09	100	2009 June 10	71		
NGC 4151	0.00332	7.66	45	33	2012 Nov 14	124	2012 Nov 14	16		
NGC 4507	0.01180	8.26	47	50	2015 June 10	68	2010 Aug 03	51		
NGC 5506	0.00618	7.94	80	40	2014 Apr 01	114	2015 July 08	322		
NGC 5643	0.00400	6.44	65	55	2014 May 24	42	2009 July 25	92		
...	2014 June 30	40		
NGC 7674	0.02892	7.56	60	40	2014 Sept 30	104	2004 June 02	22		

^aLogarithm of the mass of the black hole at the center of the AGN in solar mass. Circinus: Beifiori et al. (2012); Mrk 3, Mrk 78, Mrk 573, Mrk 1066: Nelson & Whittle (1995); Mrk 34: Gandhi et al. (2014); NGC 1068: Merritt & Ferrarese (2001); NGC 3227: Onken et al. (2003); NGC 3783: Onken & Peterson (2002); NGC 4051: Denney et al. (2009), NGC 4151: Onken et al. (2007); NGC 4507: Nicastro et al. (2003); NGC 5506: Nikolajuk et al. (2009); NGC 5643: Goulding et al. (2010); NGC 7674: Woo & Urry (2002).

^bAGN inclination angle reported in Fischer et al. (2013): 0° corresponds to an “face-on” orientation. The typical error is 5°.

^cThe opening angle between the bicone axis and the outer edge of the narrow line region, assuming a typical error of 5°.

^dTotal effective exposure time after data cleaning of *NuSTAR* FPMA and FPMB.

^eTotal effective exposure time after data cleaning of XMM-*Newton* MOS1, MOS2 and pn.

^fEffective exposure time after data cleaning for ACIS-S of *Chandra*.

source. The background spectra are extracted using a 75'' circular region near the source but avoiding contamination from it.

2.2.2. XMM-Newton

The XMM-*Newton* observations are taken with two MOS cameras (Turner et al. 2001) and the EPIC CCD cameras (pn; Strüder et al. 2001). The XMM-*Newton* data are reduced using the Science Analysis System (SAS; Jansen et al. 2001) version 17.0.0 following standard procedures. The source spectra are extracted from a circular region with radius of 15'' (corresponding to $\approx 70\%$ of the EEF at 1.5 keV) or 30'' (corresponding to $\approx 85\%$ of the EEF at 1.5 keV), based on which spectra has higher signal to noise ratio (SNR); the background spectra are extracted from a circle nearby the source with the same radius as the source spectra but avoiding contamination from sources. ARF and RMF files are produced using the tasks `arfgen` and `rmfgen`.

2.2.3. Chandra

Archived *Chandra* ACIS-S observations are used for three sources (Mrk 34, Mrk 78 and Mrk 1066) which have low-quality XMM-*Newton* data because of their short exposure time and low observing luminosity in soft X-ray band. We reduced the *Chandra* data using the *Chandra*'s data analysis system, CIAO software package (Fruscione et al. 2006) version 4.11 and *Chandra* CALDB version 4.8.2. The level = 1 data are reprocessed as suggested to apply updated calibrations as suggested using the CIAO `chandra_repro` script. The source spectrum is extracted from a circular region centered at the source with a ra-

dius of 5''; background spectrum is extracted from a circular region near the source with a radius of 10''. The CIAO `specextract` tool is used to extract both source and background spectra, ARF and RMF files following standard procedures.

The *NuSTAR*, XMM-*Newton* and *Chandra* spectra are rebinned with a minimum of 20 counts per bin using the HEASoft task `grppha`.

3. SPECTRAL ANALYSIS AND RESULTS

The spectral are fitted using the XSPEC software (Arnaud 1996) version 12.10.0c. The photoelectric cross section for the absorption component is from Verner et al. (1996); the element abundance is from Anders & Grevesse (1989) and the metal abundance is fixed to Solar; the Galactic absorption column density is obtained using the `nh` task (Kalberla et al. 2005) in HEASoft for each source. The redshift of each source is adopted from NED⁶. In this work, the spectra are analyzed using the self-consistent `borus02` model (Baloković et al. 2018), which is suitable to characterize AGNs with high-quality broadband X-ray spectra.

3.1. Spectral Modeling

The recently published Monte Carlo radiative transfer code BORUS (Baloković 2017) has already widely used to model the reprocessed component of AGN spectra (e.g., Boorman et al. 2018; La Caria et al. 2019; Kammoun et al. 2019; Li et al. 2019; Masini et al. 2019; Marchesi et al. 2019); see also the `borus02` website⁷ for more de-

⁶ <https://ned.ipac.caltech.edu>

⁷ <http://www.astro.caltech.edu/~mislavb/download/>

tails. The complete model used in fitting the spectra is composed of four parts:

1. An absorbed intrinsic continuum, described by a cut-off power-law, denoted by `cutoffpl` in `XSPEC`, multiplied by an obscuring component, considering both the photoelectric absorption (`zphabs`) and the Compton scattering (`cabs`) effects.
2. A reprocessed component produced by the obscuring material near the center of the AGN, including the scattered component and fluorescent lines, characterized by `borus02`.
3. A second, leaked unabsorbed intrinsic continuum, modeling the fractional AGN emission which is deflected, rather than absorbed by the obscuring material.
4. A thermal component, namely `mekal` (Mewe et al. 1985), modeling the soft excess observed below 1 keV, potentially describing the emission caused by the processes other than AGN, such as star formation and/or diffuse gas emission.

The reprocessed component, `borus02`⁸ assumes a sphere with conical cutouts at both poles (Baloković et al. 2018), approximating a torus with an opening angle which can vary in the range of $\theta_{\text{Tor}} = [0-84]^\circ$, corresponding to a torus covering factor, $c_f = \cos(\theta_{\text{Tor}}) = [1-0.1]$. Another parameter in the reprocessed component is the inclination angle, which is the angle between the axis of the AGN and the observer line-of-sight, $\theta_{\text{inc}} = [18-87]^\circ$, where $\theta_{\text{obs}} = 0^\circ$ is when the AGN is observed “face-on” and $\theta_{\text{obs}} = 87^\circ$ is observed “edge-on”. Another parameter, the relative iron abundance of the reprocessed component, A_{Fe} , is fixed to 1 (i.e., the iron abundance in solar, $A_{\text{Fe},\odot}$), unless a much better result is obtained leaving the parameter free to vary. We plot the spectra of the `borus02` (Baloković et al. 2018) model prediction when varying different parameters in Appendix A to illustrate how the spectra of the reprocessed component vary with different parameters, i.e., θ_{obs} , θ_{Tor} , θ_{inc} and A_{Fe} . Evidence in Infrared and X-ray observations have shown that the torus is clumpy rather than having a uniform density (e.g., Krolik & Begelman 1988; Risaliti et al. 2002; Nenkova et al. 2008; Almeida et al. 2009; Markowitz et al. 2014). Therefore, the column density of the obscuring torus in the reprocessed component is decoupled from the one in the absorbed intrinsic continuum in our modeling to approximate the clumpy nature of the obscuring torus. In this scenario, the column density of the reprocessed component is an average property of the clumpy torus while the column density of the absorbed intrinsic continuum represents a line-of-sight quantity.

In the process of modeling the spectra, the photon index, Γ , the cut-off energy, E_{cut} and the normalization, $norm$, of the intrinsic continuum, the reprocessed component and the fractional unabsorbed continuum are tied together, assuming that the three component have the same origin. The cut-off energy is fixed at $E_{\text{cut}} =$

500 keV, unless a much better result is obtained leaving the parameter free to vary. The fractional unabsorbed continuum is usually less than 5–10% of the intrinsic continuum (see, e.g., Noguchi et al. 2010; Marchesi et al. 2018). We denote this fraction as f_s , and we model it with a constant (`constant2`). Finally, the temperature and the relative metal abundance in `mekal` are both left free to vary. Lines are added if strong emission lines are found in the spectra using `zgauss` model in `XSPEC`.

The `borus02` model is used in the following `XSPEC` configuration:

$$\text{Model} = \text{constant}_1 * \text{phabs} * (\text{borus02} + \text{zphabs} * \text{cabs} * \text{cutoffpl} + \text{constant}_2 * \text{cutoffpl} + \text{mekal})$$

where `constant1` is the cross-calibration between *NuSTAR* and *XMM-Newton* (separate cross-calibration constants are applied if *Chandra* data are used); `phabs` models the Galactic absorption.

3.2. Results

We fit the spectra twice at first: letting the inclination angle free to vary when fitting the spectra and fixing the inclination angle at the values reported in Fischer et al. (2013). The best-fit results are reported in Table 2 and Table 3. Furthermore, to extend our analysis on the role of inclination angle in the spectral analysis, we also fit the spectra by fixing the inclination at some specific angles, i.e., $\theta_{\text{inc}} = 60^\circ$ or $\cos(\theta_{\text{inc}}) = 0.5$ (i.e., the opening angle of the torus in MYTorus model Murphy & Yaqoob 2009), and fixing inclination at $\theta_{\text{inc}} = 87^\circ$ (the maximum angle in `borus02` model) representing an “edge-on” scenario, which is commonly used when analyzing heavily obscured AGN spectra (see, e.g., Brightman & Nandra 2011; Koss et al. 2015; Ricci et al. 2016; Marchesi et al. 2018; Zappacosta et al. 2018), although not all of the sources in our sample are heavily obscured. The best-fit results of the two scenarios are also reported in Table 2 and Table 3. The details of fitting procedure of each source and best-fit results of the 13 sources fitted when the inclination angles are left free to vary are reported in Appendix C. The unfolded spectra and the model predictions of each source when fitted leaving the inclination angle free to vary are plotted in Appendix C as well.

6 out of 13 sources in our sample have been observed displaying strong variability between their soft X-ray observations and *NuSTAR* observations. The observed variability is commonly explained by either the variation of the accretion rate of the SMBH or the variation in the so-called corona when the fluctuation of intrinsic emission of the AGN is observed, i.e., the shape of the spectrum does not change while the normalization of the intrinsic power-law varies (Nandra 2001), or the change in the absorption column density along the line-of-sight when the shape of the spectra varies (see, e.g., Risaliti et al. 2002; Bianchi et al. 2012), or both. To properly characterize the spectra of these sources, we fit them three times: 1. disentangling the normalization of the intrinsic cut-off power law, `norm`, of the soft X-ray observatories observations and the *NuSTAR* observations, modeling the flux variability caused by the intrinsic emission variation; 2. disentangling the line-of-sight column densities of the soft X-ray observations, $N_{\text{H,los,soft}}$ and *NuSTAR* observations, $N_{\text{H,los,NuS}}$, model-

⁸ The energy coverage of `borus02` model is $1 \text{ keV} < E < 1000 \text{ keV}$. The model cut-off at 1 keV does not affect the fit of the sources in our sample since their spectra in soft energy band ($E < 3 \text{ keV}$) are dominated by the leaked component.

Table 2
Best-fit results of 13 sources

Model	$\chi^2/\text{d.o.f.}$	Γ	$N_{\text{H},\text{l.o.s.}}^{\text{a}}$	$N_{\text{H},\text{tor}}^{\text{b}}$	$\cos(\theta_{\text{inc}})^{\text{c}}$	$c_{\text{f},\text{tor}}^{\text{d}}$	norm^{e}	f_s^{f}	F_{2-10}^{g}	$L_{\text{int}}^{\text{h}}$
Mrk 3										
free	1056/1073	$1.48_{-u}^{+0.11}$	$23.94_{-0.04}^{+0.06}$	$23.30_{-0.15}^{+0.24}$	$0.47_{-0.07}^{+0.16}$	$0.50_{-0.22}^{+0.06}$	$1.42_{-0.22}^{+0.54}$	$0.98_{-0.89}^{+0.46}$	8_{-4}^{+1}	31
[OIII]	1061/1074	$1.40_{-u}^{+0.05}$	$23.91_{-0.05}^{+0.01}$	$23.04_{-0.26}^{+0.24}$	0.09^f	$0.62_{-0.05}^{+0.28}$	$1.12_{-0.11}^{+0.01}$	$1.36_{-0.14}^{+0.55}$	8_{-4}^{+2}	28
60°	1057/1074	$1.46_{-u}^{+0.18}$	$23.95_{-0.05}^{+0.06}$	$23.32_{-0.24}^{+0.44}$	0.50^f	$0.50_{-0.17}^{+0.06}$	$1.35_{-0.17}^{+0.82}$	$0.81_{-0.50}^{+0.36}$	8_{-5}^{+1}	31
87°	1061/1074	$1.40_{-u}^{+0.12}$	$23.90_{-0.04}^{+0.02}$	$23.07_{-0.31}^{+0.19}$	0.05^f	$0.60_{-0.04}^{+0.29}$	$1.12_{-0.11}^{+0.01}$	$1.41_{-0.14}^{+0.44}$	8_{-3}^{+3}	28
Mrk 34										
free	74/82	$1.45_{-u}^{+0.67}$	$24.74_{-0.46}^{+u}$	$25.04_{-0.73}^{+u}$	0.42_{-u}^{+u}	$0.40_{-0.27}^{+0.44}$	$0.06_{-0.03}^{+0.35}$	$0.85_{-0.65}^{+2.02}$	$0.2_{-0.2}^{+18}$	21
[OIII]	74/83	$1.49_{-u}^{+0.59}$	$24.73_{-0.34}^{+u}$	$24.98_{-0.64}^{+u}$	0.42^f	$0.41_{-0.31}^{+0.06}$	$0.07_{-0.02}^{+0.56}$	$0.74_{-0.53}^{+0.53}$	$0.2_{-0.2}^{+3.7}$	24
60°	74/83	$1.46_{-u}^{+0.55}$	$24.67_{-0.36}^{+u}$	$25.00_{-0.71}^{+u}$	0.50^f	$0.43_{-u}^{+0.09}$	$0.05_{-0.10}^{+0.47}$	$1.12_{-0.82}^{+0.65}$	$0.2_{-0.2}^{+2.2}$	16
87°	76/83	$1.41_{-u}^{+0.33}$	$24.59_{-0.04}^{+0.08}$	$23.66_{-0.09}^{+0.17}$	0.05^f	$0.10_{-u}^{+0.13}$	$0.25_{-0.02}^{+0.07}$	$0.29_{-0.05}^{+0.06}$	$0.2_{-0.2}^{+0.5}$	96
Mrk 78										
free	276/271	$1.40_{-u}^{+0.21}$	$23.91_{-0.02}^{+0.13}$	$24.21_{-0.33}^{+0.18}$	$0.43_{-0.18}^{+0.45}$	$0.45_{-0.23}^{+u}$	$0.06_{-0.03}^{+0.00}$	$1.80_{-0.20}^{+2.00}$	$0.5_{-0.5}^{+0.3}$	12
[OIII]	276/272	$1.40_{-u}^{+0.22}$	$23.89_{-0.07}^{+0.07}$	$24.15_{-0.25}^{+0.15}$	0.50^f	$0.54_{-0.12}^{+u}$	$0.05_{-0.01}^{+0.00}$	$2.19_{-0.23}^{+1.56}$	$0.5_{-0.5}^{+0.2}$	10
60°	276/272	$1.40_{-u}^{+0.22}$	$23.89_{-0.07}^{+0.07}$	$24.15_{-0.25}^{+0.15}$	0.50^f	$0.54_{-0.12}^{+u}$	$0.05_{-0.01}^{+0.00}$	$2.19_{-0.23}^{+1.56}$	$0.5_{-0.5}^{+0.2}$	10
87°	278/272	$1.40_{-u}^{+0.16}$	$23.82_{-0.02}^{+0.06}$	$23.95_{-0.06}^{+0.07}$	0.05^f	$0.99_{-0.34}^{+u}$	$0.04_{-0.01}^{+0.00}$	$3.32_{-0.29}^{+0.90}$	$0.5_{-0.3}^{+0.1}$	8.0
Mrk 573										
free	152/194	$2.35_{-0.65}^{+u}$	$24.52_{-0.30}^{+u}$	$24.91_{-0.68}^{+u}$	0.60_{-u}^{+u}	$0.61_{-u}^{+0.37}$	$0.56_{-0.51}^{+2.25}$	$0.17_{-0.19}^{+1.91}$	$0.3_{-0.3}^{+10}$	5.7
[OIII]	152/195	$2.36_{-0.62}^{+u}$	$24.63_{-0.32}^{+u}$	$25.00_{-0.73}^{+u}$	0.50^f	$0.54_{-u}^{+0.04}$	$0.96_{-0.87}^{+2.58}$	$0.10_{-0.10}^{+1.13}$	$0.3_{-0.3}^{+12}$	9.7
60°	152/195	$2.36_{-0.62}^{+u}$	$24.63_{-0.32}^{+u}$	$25.00_{-0.73}^{+u}$	0.50^f	$0.54_{-u}^{+0.04}$	$0.96_{-0.87}^{+2.58}$	$0.10_{-0.10}^{+1.13}$	$0.3_{-0.3}^{+12}$	9.7
87°	152/195	$2.60_{-0.02}^{+u}$	$24.94_{-0.05}^{+u}$	$24.99_{-0.02}^{+0.04}$	0.05^f	$0.12_{-u}^{+0.06}$	110_{-8}^{+6}	$0.00_{-0.00}^{+0.01}$	$0.3_{-0.3}^{+1.1}$	798
Mrk 1066										
free	142/147	$1.52_{-u}^{+0.02}$	$23.97_{-0.05}^{+0.03}$	$24.16_{-0.10}^{+0.31}$	0.65_{-u}^{+u}	$1.00_{-0.36}^{+u}$	$0.08_{-0.01}^{+0.11}$	$4.05_{-2.36}^{+2.38}$	$0.3_{-0.3}^{+0.1}$	1.1
[OIII]	142/148	$1.53_{-0.06}^{+0.06}$	$23.98_{-0.07}^{+0.03}$	$24.17_{-0.05}^{+0.06}$	0.17^f	$1.00_{-0.37}^{+u}$	$0.08_{-0.01}^{+0.02}$	$4.04_{-0.47}^{+1.51}$	$0.3_{-0.3}^{+0.1}$	1.1
60°	142/148	$1.54_{-0.04}^{+0.02}$	$23.98_{-0.02}^{+0.00}$	$24.17_{-0.02}^{+0.01}$	0.50^f	$1.00_{-0.36}^{+u}$	$0.09_{-0.00}^{+0.01}$	$3.78_{-0.08}^{+0.63}$	$0.3_{-0.3}^{+0.1}$	1.2
87°	142/148	$1.53_{-0.03}^{+0.06}$	$23.97_{-0.06}^{+0.04}$	$24.17_{-0.07}^{+0.04}$	0.05^f	$1.00_{-0.36}^{+u}$	$0.09_{-0.03}^{+0.10}$	$3.78_{-0.70}^{+2.32}$	$0.3_{-0.3}^{+0.1}$	1.2
NGC 3227										
free	4684/4008	$1.68_{-0.01}^{+0.01}$	$21.39_{-0.01}^{+0.03}$	$23.14_{-0.02}^{+0.03}$	$0.15_{-u}^{+0.14}$	$1.00_{-0.07}^{+u}$	$0.86_{-0.01}^{+0.01}$	0^f	$37.7_{-0.2}^{+0.3}$	1.2
[OIII]	4686/4009	$1.68_{-0.01}^{+0.01}$	$21.39_{-0.04}^{+0.05}$	$23.14_{-0.04}^{+0.03}$	0.95^f	$1.00_{-0.05}^{+u}$	$0.86_{-0.01}^{+0.01}$	0^f	$37.7_{-0.1}^{+0.2}$	1.2
60°	4686/4009	$1.68_{-0.01}^{+0.01}$	$21.39_{-0.06}^{+0.05}$	$23.14_{-0.04}^{+0.03}$	0.95^f	$1.00_{-0.13}^{+u}$	$0.86_{-0.01}^{+0.01}$	0^f	$37.7_{-0.1}^{+0.1}$	1.2
87°	4686/4009	$1.68_{-0.01}^{+0.01}$	$21.39_{-0.06}^{+0.05}$	$23.15_{-0.04}^{+0.03}$	0.05^f	$1.00_{-0.11}^{+u}$	$0.87_{-0.02}^{+0.01}$	0^f	$37.7_{-0.3}^{+0.3}$	1.2
NGC 3783										
free	3349/2929	$1.51_{-0.04}^{+0.02}$	$22.85_{-0.01}^{+0.01}$	$25.00_{-0.22}^{+0.11}$	$0.54_{-0.02}^{+0.02}$	$0.41_{-0.04}^{+0.08}$	$0.68_{-0.03}^{+0.03}$	$10.14_{-0.28}^{+0.30}$	26_{-1}^{+1}	6.9
[OIII]	3367/2930	$1.49_{-0.02}^{+0.04}$	$22.84_{-0.01}^{+0.02}$	$25.11_{-0.23}^{+u}$	0.95^f	$0.26_{-0.01}^{+0.01}$	$0.66_{-0.03}^{+0.05}$	$10.55_{-0.70}^{+0.39}$	26_{-2}^{+1}	6.9
60°	3356/2930	$1.49_{-0.05}^{+0.01}$	$22.85_{-0.01}^{+0.01}$	$24.98_{-0.27}^{+0.12}$	0.50^f	$0.40_{-0.02}^{+0.01}$	$0.67_{-0.05}^{+0.02}$	$10.42_{-0.33}^{+0.11}$	26_{-2}^{+1}	6.9
87°	3439/2930	$1.55_{-0.01}^{+0.01}$	$22.82_{-0.01}^{+0.01}$	$23.58_{-0.08}^{+0.06}$	0.05^f	$1.00_{-0.03}^{+u}$	$0.66_{-0.04}^{+0.01}$	$10.47_{-0.18}^{+0.69}$	27_{-1}^{+0}	6.8

^aLogarithm of line-of-sight column density in cm^{-2} ; for sources which variability has been observed between the *NuSTAR* and *XMM-Newton*, we report here the line-of-sight column density of the *XMM-Newton* observation

^bLogarithm of average torus column density in cm^{-2}

^cInclination angle, i.e., the angle between the axis of the torus and the edge of the torus

^dEffective covering factor of the torus

^eNormalization of the main cut-off power-law component at 1 keV in 10^{-2} photons $\text{keV}^{-1} \text{cm}^{-2} \text{s}^{-1}$ of *XMM-Newton* observations

^fFraction of scattering component in 10^{-2}

^gFlux between 2–10 keV in $10^{-12} \text{erg cm}^{-2} \text{s}^{-1}$ of *XMM-Newton* observation

^hIntrinsic luminosity between 2–10 keV in $10^{42} \text{erg s}^{-1}$ of *XMM-Newton* observation

Table 3
Best-fit results of 13 sources

Model	$\chi^2/\text{d.o.f.}$	Γ	$N_{\text{H,l.o.s}}^{\text{a}}$	$N_{\text{H,tor}}^{\text{b}}$	$\cos(\theta_{\text{inc}})^{\text{c}}$	$c_{\text{f,tor}}^{\text{d}}$	norm ^e	f_s^{f}	F_{2-10}^{g}	$L_{\text{int}}^{\text{h}}$
NGC 4051										
free	2686/2390	$1.72^{+0.01}_{-0.01}$	$22.53^{+0.01}_{-0.01}$	$24.45^{+0.07}_{-0.09}$	$0.95^{+u}_{-0.01}$	$0.95^{+0.01}_{-0.01}$	$0.45^{+0.01}_{-0.01}$	0^f	14^{+1}_{-1}	0.2
[OIII]	2686/2391	$1.72^{+0.01}_{-0.01}$	$22.53^{+0.01}_{-0.01}$	$24.45^{+0.07}_{-0.06}$	0.95^f	$0.95^{+0.01}_{-0.01}$	$0.45^{+0.01}_{-0.01}$	0^f	14^{+1}_{-1}	0.2
60°	2739/2391	$1.70^{+0.03}_{-0.05}$	$22.53^{+0.03}_{-0.02}$	$24.16^{+0.03}_{-0.04}$	0.50^f	$1.00^{+u}_{-0.04}$	$0.45^{+0.01}_{-0.02}$	0^f	14^{+0}_{-2}	0.2
87°	2738/2391	$1.70^{+0.03}_{-0.05}$	$22.53^{+0.03}_{-0.01}$	$24.16^{+0.03}_{-0.05}$	0.05^f	$1.00^{+u}_{-0.02}$	$0.45^{+0.01}_{-0.02}$	0^f	14^{+0}_{-2}	0.2
NGC 4151										
free	5200/4664	$1.67^{+0.02}_{-0.04}$	$23.00^{+0.01}_{-0.01}$	$23.94^{+0.02}_{-0.02}$	$0.05^{+0.03}_{-u}$	$0.80^{+0.04}_{-0.07}$	$3.64^{+0.16}_{-0.23}$	$2.75^{+0.20}_{-0.13}$	88^{+1}_{-1}	3.6
[OIII]	5208/4665	$1.74^{+0.02}_{-0.01}$	$23.01^{+0.01}_{-0.00}$	$24.01^{+0.04}_{-0.03}$	0.71^f	$0.88^{+u}_{-0.06}$	$4.09^{+0.19}_{-0.12}$	$2.49^{+0.11}_{-0.14}$	88^{+1}_{-1}	3.7
60°	5201/4665	$1.69^{+0.03}_{-0.04}$	$23.00^{+0.02}_{-0.01}$	$23.98^{+0.02}_{-0.02}$	0.50^f	$0.78^{+0.08}_{-0.09}$	$3.75^{+0.22}_{-0.27}$	$2.68^{+0.23}_{-0.16}$	88^{+1}_{-1}	3.6
87°	5200/4665	$1.67^{+0.02}_{-0.04}$	$23.00^{+0.01}_{-0.01}$	$23.94^{+0.04}_{-0.03}$	0.05^f	$0.80^{+0.04}_{-0.06}$	$3.64^{+0.16}_{-0.24}$	$2.75^{+0.20}_{-0.13}$	88^{+1}_{-1}	3.6
NGC 4507										
free	1601/1614	$1.71^{+0.05}_{-0.03}$	$23.98^{+0.03}_{-0.05}$	$23.40^{+0.09}_{-0.09}$	$0.43^{+0.10}_{-0.13}$	$0.55^{+0.09}_{-0.06}$	$2.03^{+0.40}_{-0.46}$	$0.27^{+0.18}_{-0.19}$	$7.1^{+0.3}_{-0.3}$	25
[OIII]	1603/1615	$1.85^{+0.04}_{-0.02}$	$23.87^{+0.02}_{-0.02}$	$25.50^{+u}_{-0.19}$	0.68^f	$0.40^{+0.06}_{-0.06}$	$1.67^{+0.24}_{-0.10}$	$0.18^{+0.15}_{-0.02}$	$7.1^{+0.2}_{-0.3}$	17
60°	1603/1615	$1.68^{+0.02}_{-0.05}$	$23.98^{+0.02}_{-0.06}$	$23.44^{+0.04}_{-0.11}$	0.50^f	$0.59^{+0.07}_{-0.04}$	$1.81^{+0.14}_{-0.34}$	$0.23^{+0.17}_{-0.18}$	$7.1^{+0.2}_{-0.3}$	23
87°	1607/1615	$1.69^{+0.06}_{-0.04}$	$23.97^{+0.05}_{-0.03}$	$23.34^{+0.06}_{-0.05}$	0.05^f	$0.63^{+0.08}_{-0.05}$	$1.89^{+0.52}_{-0.29}$	$0.43^{+0.10}_{-0.09}$	$7.1^{+0.1}_{-0.3}$	24
NGC 5506										
free	5378/4543	$1.72^{+0.01}_{-0.01}$	$22.50^{+0.01}_{-0.00}$	$23.91^{+0.02}_{-0.02}$	$0.55^{+0.09}_{-0.25}$	$1.00^{+u}_{-0.02}$	$1.90^{+0.03}_{-0.01}$	$1.33^{+0.04}_{-0.04}$	61^{+4}_{-0}	4.9
[OIII]	5381/4544	$1.72^{+0.02}_{-0.01}$	$22.50^{+0.01}_{-0.00}$	$23.91^{+0.01}_{-0.01}$	0.17^f	$1.00^{+u}_{-0.02}$	$1.90^{+0.04}_{-0.03}$	$1.33^{+0.04}_{-0.05}$	61^{+4}_{-1}	4.9
60°	5379/4544	$1.72^{+0.01}_{-0.01}$	$22.50^{+0.01}_{-0.00}$	$23.91^{+0.02}_{-0.02}$	0.50^f	$1.00^{+u}_{-0.02}$	$1.90^{+0.03}_{-0.02}$	$1.33^{+0.04}_{-0.05}$	61^{+4}_{-0}	4.9
87°	5380/4544	$1.72^{+0.02}_{-0.01}$	$22.50^{+0.01}_{-0.00}$	$23.91^{+0.01}_{-0.01}$	0.05^f	$1.00^{+u}_{-0.02}$	$1.90^{+0.04}_{-0.03}$	$1.33^{+0.04}_{-0.05}$	61^{+5}_{-1}	4.9
NGC 5643										
free	198/170	$1.77^{+0.27}_{-0.37}$	$24.65^{+u}_{-0.32}$	$24.15^{+0.22}_{-0.35}$	$0.51^{+u}_{-0.24}$	$0.50^{+0.38}_{-0.23}$	$0.41^{+1.23}_{-0.27}$	$0.10^{+0.39}_{-0.10}$	$0.8^{+15}_{-0.6}$	0.5
[OIII]	199/171	$1.77^{+0.32}_{-0.34}$	$24.65^{+0.23}_{-0.25}$	$24.13^{+0.23}_{-0.28}$	0.42^f	$0.42^{+0.04}_{-0.13}$	$0.51^{+0.63}_{-0.28}$	$0.08^{+0.28}_{-0.08}$	$0.8^{+19}_{-0.3}$	0.6
60°	198/171	$1.80^{+0.27}_{-0.32}$	$24.65^{+u}_{-0.28}$	$24.15^{+0.24}_{-0.31}$	0.50^f	$0.49^{+0.04}_{-0.12}$	$0.47^{+0.54}_{-0.25}$	$0.10^{+0.31}_{-0.10}$	$0.8^{+17}_{-0.5}$	0.6
87°	220/171	$1.40^{+0.12}_{-u}$	$24.35^{+0.06}_{-0.05}$	$23.44^{+0.04}_{-0.08}$	0.05^f	$0.43^{+0.03}_{-0.07}$	$0.12^{+0.01}_{-0.01}$	$1.59^{+0.21}_{-0.21}$	$0.8^{+0.4}_{-0.6}$	0.3
NGC 7674										
free	240/251	$2.21^{+0.12}_{-0.18}$	$24.15^{+0.08}_{-0.05}$	$23.65^{+0.14}_{-0.05}$	$0.25^{+0.52}_{-0.04}$	$0.10^{+0.15}_{-u}$	$1.49^{+2.87}_{-0.06}$	0^f	$0.6^{+0.6}_{-0.6}$	54
[OIII]	241/252	$2.20^{+0.17}_{-0.19}$	$24.13^{+0.06}_{-0.06}$	$23.73^{+0.11}_{-0.05}$	0.50^f	$0.10^{+0.07}_{-u}$	$1.26^{+0.36}_{-0.06}$	0^f	$0.7^{+0.2}_{-0.7}$	46
60°	241/252	$2.20^{+0.17}_{-0.19}$	$24.13^{+0.06}_{-0.06}$	$23.73^{+0.11}_{-0.05}$	0.50^f	$0.10^{+0.07}_{-u}$	$1.26^{+0.36}_{-0.06}$	0^f	$0.7^{+0.2}_{-0.7}$	46
87°	245/251	$2.00^{+0.40}_{-0.31}$	$24.10^{+0.15}_{-0.17}$	$23.27^{+0.13}_{-0.18}$	0.05^f	$0.30^{+0.39}_{-u}$	$0.66^{+1.65}_{-0.49}$	$0.60^{+1.47}_{-0.04}$	$0.7^{+0.1}_{-0.7}$	32

^aLogarithm of line-of-sight column density in cm^{-2} ; for sources which variability has been observed between the *NuSTAR* and *XMM-Newton*, we report here the line-of-sight column density of the *XMM-Newton* observation

^bLogarithm of average torus column density in cm^{-2}

^cInclination angle, i.e., the angle between the axis of the torus and the edge of the torus

^dEffective covering factor of the torus

^enormalization of the main cut-off power-law component at 1 keV in 10^{-2} photons $\text{keV}^{-1} \text{cm}^{-2} \text{s}^{-1}$ of *XMM-Newton* observations

^fFraction of scattering component in 10^{-2}

^gFlux between 2–10 keV in $10^{-12} \text{erg cm}^{-2} \text{s}^{-1}$ of *XMM-Newton* observation

^hIntrinsic luminosity between 2–10 keV in $10^{42} \text{erg s}^{-1}$ of *XMM-Newton* observation

ing the flux variability results from the line-of-sight column density variability; 3. disentangling both the norm and $N_{\text{H,los}}$ between the soft X-ray observations and the *NuSTAR* observations, assuming the flux variability is caused by both the intrinsic emission variation and line-of-sight column density variability. Here, we treat the reprocessed emission as an invariable component during the two observations, assuming a stable structure and constant global properties of the obscuring torus.

The decoupling line-of-sight column density and the torus average column density applied to fit the spectra in this work is commonly used to approximate the non-uniform (clumpy) torus. To interpret the obtained results, we separate the sources in three categories.

1. Obscured AGNs with $\log(N_{\text{H,l.o.s}}) \geq 22$ where the line-of-sight does not intercept the torus ($\cos(\theta_{\text{inc}}) > c_{\text{f,tor}}$), i.e., Mrk 34, NGC 3783, NGC 5643. The interpretation of this result is that an obscured clump is above the torus along our line-of-sight. However, we cannot exclude the possibility that the inclination angle smaller than the half-opening angle of the torus ($\cos(\theta_{\text{inc}}) > c_{\text{f,tor}}$) may correspond to a clumpy torus seen edge-on (see, Fig. 3 and Section 2.3 in Baloković et al. 2018) and (Fig. 6.1 in Baloković 2017).
2. Unobscured AGN $\log(N_{\text{H,l.o.s}}) < 22$ where the line-of-sight intercept the torus ($\cos(\theta_{\text{inc}}) \leq c_{\text{f,tor}}$), i.e., NGC 3227. This result may suggest that the source is observed through an underdense region of a clumpy obscured torus.
3. Obscured AGNs with their line-of-sight intercepting the torus but the line-of-sight column density is significantly different from the torus average column density ($|\Delta \log(N_{\text{H}})| \gtrsim 1$), e.g., NGC 3227, NGC 4051, NGC 4151 and NGC 5506. This result shows that we are currently looking through either an overdense or underdense region in their non-uniform tori, and this could be changing with time (see, e.g., Risaliti et al. 2005).

4. DISCUSSION

Thanks to the *borus02* model and the [OIII] measured inclination, we are able to properly study the role of inclination angle in analyzing the AGN spectra: the best-fit results of 13 sources when fitted with different scenarios of applying the inclination angle are reported in Section 3. In the rest of the work, we discuss how varying the inclination angle affects the measurement of the other spectral parameters (Section 4.1, Section 4.2 and Section 4.3), the correlations between the covering factor of the obscuring torus and other AGN properties (Section 4.4), and study the geometrical properties of the AGNs in both X-ray and optical (Section 4.5).

4.1. Fixing the Torus Inclination Angle at $\theta_{\text{inc,[OIII]}}$

We compare the best-fit results of different spectral parameters (i.e., $\chi^2/\text{d.o.f.}$, Γ , $N_{\text{H,l.o.s}}$, $N_{\text{H,tor}}$, $c_{\text{f,tor}}$ and θ_{inc}), computed either leaving the inclination angle free to vary or using the [OIII] measured values, $\theta_{\text{inc,[OIII]}}$, reported in Fischer et al. (2013). The best-fit results

Table 4
Average uncertainties of different parameters assuming different torus inclination angles

Parameter	Free to vary	[OIII]	60°	87°
Γ	10%	9%	10%	6%
$N_{\text{H,l.o.s}}$	19%	18%	18%	10%
$N_{\text{H,tor}}$	38%	36%	37%	17%
$c_{\text{f,tor}}^{\text{a}}$	0.17	0.11	0.11	0.10
χ^2_{ν}	1.04	1.04	1.04	1.05

^aAbsolute average uncertainty

obtained in two scenarios are reported in Table 2 and Table 3. We compare the best-fit $c_{\text{f,tor}}$ and $N_{\text{H,tor}}$ computed in two methods in Fig. 2. The above comparison is also plotted as an histogram in Figure 1 for better readability.

- The inclination angles of 3 sources in our sample (Mrk 34, Mrk 573 and Mrk 1066) are fully unconstrained when inclination angle is left free to vary in fitting the spectra due to the poor quality (d.o.f ≤ 200) of the data.

The best-fit inclination angles measured in X-ray do not always match the inclination angles measured in optical using [OIII], e.g., we found 6 sources of which the differences between the two inclination angles is $\Delta\theta_{\text{inc}} > 20^\circ$.

- In spite of large $\Delta\theta_{\text{inc}}$ found in some sources, the best-fit results of the other key parameters, e.g., $N_{\text{H,l.o.s}}$, $N_{\text{H,tor}}$ and $c_{\text{f,tor}}$ are in good agreement with each other within the uncertainties.
- The goodness of the spectral fits shows no improvement or only a marginal improvement when inclination angle is left free to vary in fitting the spectra. The sources with most improved fit statistics in our sample is NGC 3783, which improves from $\chi^2/\text{d.o.f} = 3367/2930$ when fixing the inclination angle at the [OIII] measured inclination to $\chi^2/\text{d.o.f} = 3349/2929$ when letting the inclination free to vary.
- A minor improvement on constraining the spectral parameters are found when fixing the θ_{inc} at [OIII] measured value. The average uncertainties on each parameters are reported in Table 4.

The above results suggest that: 1. the inclination angle measured in the optical band using [OIII] can be used in the X-ray spectral analysis of AGNs, since it provides similar best-fit results to those obtained when inclination angle is left free to vary when fitting the spectra considering uncertainties; 2. in some sources, significant different inclination angles measured in the optical compared to those derived from the X-ray spectra are found, but the other fitted parameters, as well as the best-fit statistic, are only marginally affected by this variation, suggesting that we do not have enough power to constrain the inclination angle of these sources even with high-quality broadband X-ray data.

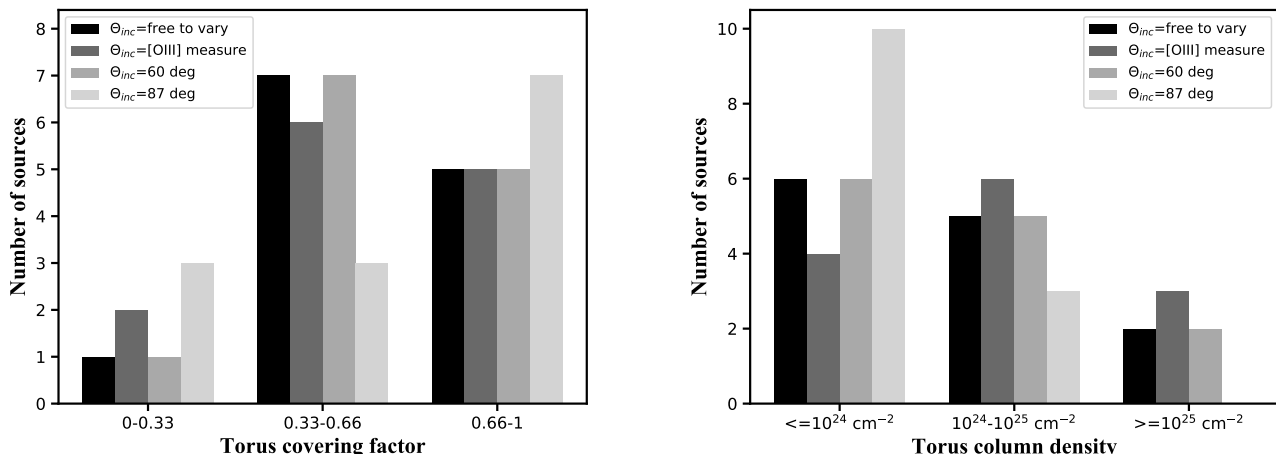


Figure 1. The figures from the left to right in the first row are the number of sources with specific best-fit torus covering factor and torus column density when θ_{inc} is left free to vary (black histogram), when θ_{inc} is fixed at [OIII] measured values (dark gray histogram), when θ_{inc} is fixed at $\theta_{inc} = 60^\circ$ (light gray histogram) and $\theta_{inc} = 87^\circ$ (silver histogram).

4.2. Fixing the Torus Inclination Angle at $\theta_{inc} = 60^\circ$

Following the method in Section 4.1, we compare the best-fit results obtained when leaving the inclination angle free to vary with the best-fit results computed when fixing the inclination at some specific angles, e.g., $\theta_{inc} = 60^\circ$. The best-fit results when the sources are fitted with $\theta_{inc} = 60^\circ$ is reported in Table 2 and Table 3. The comparison of $c_{f,tor}$ and $N_{H,tor}$ between the two scenarios are plotted in Figure 2. The above comparison is also plotted as a histogram in Figure 1 for better readability.

We find that the differences of the best-fit results of different parameters between when $\theta_{inc} = 60^\circ$ and when leaving θ_{inc} free to vary are marginal, e.g., the average differences are $\sim 1\%$ for Γ , $\sim 2\%$ for $N_{H,l.o.s.}$, $\sim 5\%$ for $N_{H,tor}$ and 2% for $c_{f,tor}$. We measure a similar average goodness of fitting in the two scenarios as reported in Table 4. Only marginal improvements are found in the fits of most sources when inclination angle is left free to vary in fitting the spectra than the inclination angle is fixed at $\theta_{inc} = 60^\circ$, except for NGC 4051, whose fit improves from $\chi^2/d.o.f = 2739/2391$ to $\chi^2/d.o.f = 2686/2390$ after letting the inclination free to vary. Fixing the inclination angle at $\theta_{inc} = 60^\circ$ provides similar constraints on fitting which are consistent with those obtained when fixing θ_{inc} at [OIII] measured values.

Although, according to our spectral fits, fixing the inclination angle at $\theta_{inc} = 60^\circ$ provides similar goodness of fits and similar other key properties to those when θ_{inc} is left free to vary, this results may be biased by the sample that we have selected, since 9 out of 13 sources in our sample have a $\theta_{inc} \sim 60^\circ$. Indeed, we find that fixing the inclination angle at $\theta_{inc} = 60^\circ$ does not reproduce the $N_{H,tor}$ and other key parameters measured when θ_{inc} is left free to vary in some heavily obscured sources out of our sample, e.g., we reanalyze the spectra of a Compton thick (CT-) AGN, NGC 1358, and the best-fit $N_{H,tor}$ and $c_{f,tor}$ obtained when fixing the inclination angle at $\theta_{inc} = 60^\circ$ is about 5 times larger than those obtained when the inclination is left free to vary as reported in Zhao et al. (2019b), which measured a best-fit inclination angle of $\theta_{inc,NGC1358} \approx 87^\circ$.

4.3. Fixing the Torus Inclination Angle at $\theta_{inc} = 87^\circ$

We also fit the spectra when fixing the inclination angle at $\theta_{inc} = 87^\circ$. The differences of the best-fit results of Γ and $N_{H,l.o.s.}$ between obtained when $\theta_{inc} = 87^\circ$ and when leaving θ_{inc} free to vary are marginal, e.g., the average differences are $\sim 2\%$ for Γ , $\sim 9\%$ for $N_{H,l.o.s.}$. However, the measurement of $N_{H,tor}$ when $\theta_{inc} = 87^\circ$, especially for some sources with CT torus (i.e., $\log(N_{H,tor}) \gg 24$), are considerably different (the average difference is $\sim 30\%$) from those obtained when θ_{inc} is left free to vary. The discrepancy of $c_{f,tor}$ between the two cases is large as well, e.g., the average difference is 22%. However, unlike the $N_{H,tor}$ case where the measurements of higher $N_{H,tor}$ tend to a lower value, such trend is not found in $c_{f,tor}$. Notably, $\sim 30\%$ of the sources in our sample are measured with best-fit photon indices stuck at $\Gamma \sim 1.4$, which is the lower limit of the parameter in *borus02* model. Such a result can be explained by the fact that a flatter Γ is needed to compensate the change of the spectral shape caused by the unrealistic measurement of $c_{f,tor}$ and $N_{H,tor}$. It is worth noting that fixing the inclination angle at $\theta_{inc} = 87^\circ$ leads to significant different best-fit torus covering factor and torus column density than when the inclination angle is left free to vary even when fitting the CT-AGNs, which are plot in red in Fig. 2.

To illustrate the torus column density bias mentioned above, we take NGC 5643 as an example. The source is a CT-AGN and the spectrum of the source is dominated by reprocessed component. We plot the spectra and different components of the model predictions of NGC 5643 with inclination angle being fixed at $\theta_{inc} = 87^\circ$ and being left free to vary in Fig. 3. The best-fit inclination angle measured for NGC 5643 is $\theta_{inc} \sim 59^\circ$. When the inclination is left free to vary, the spectra above 2 keV are dominated by the reprocessed component and the measured best-fit torus column density is $\log(N_{H,tor,free}) \sim 24.15$. However, when the inclination angle is fixed at $\theta_{inc} = 87^\circ$, the best-fit torus column density is measured as $\log(N_{H,tor,free}) \sim 23.44$. Such result can be understood by looking at the bottom left panel of Fig. 3, where we plot the *borus02* model prediction of the re-

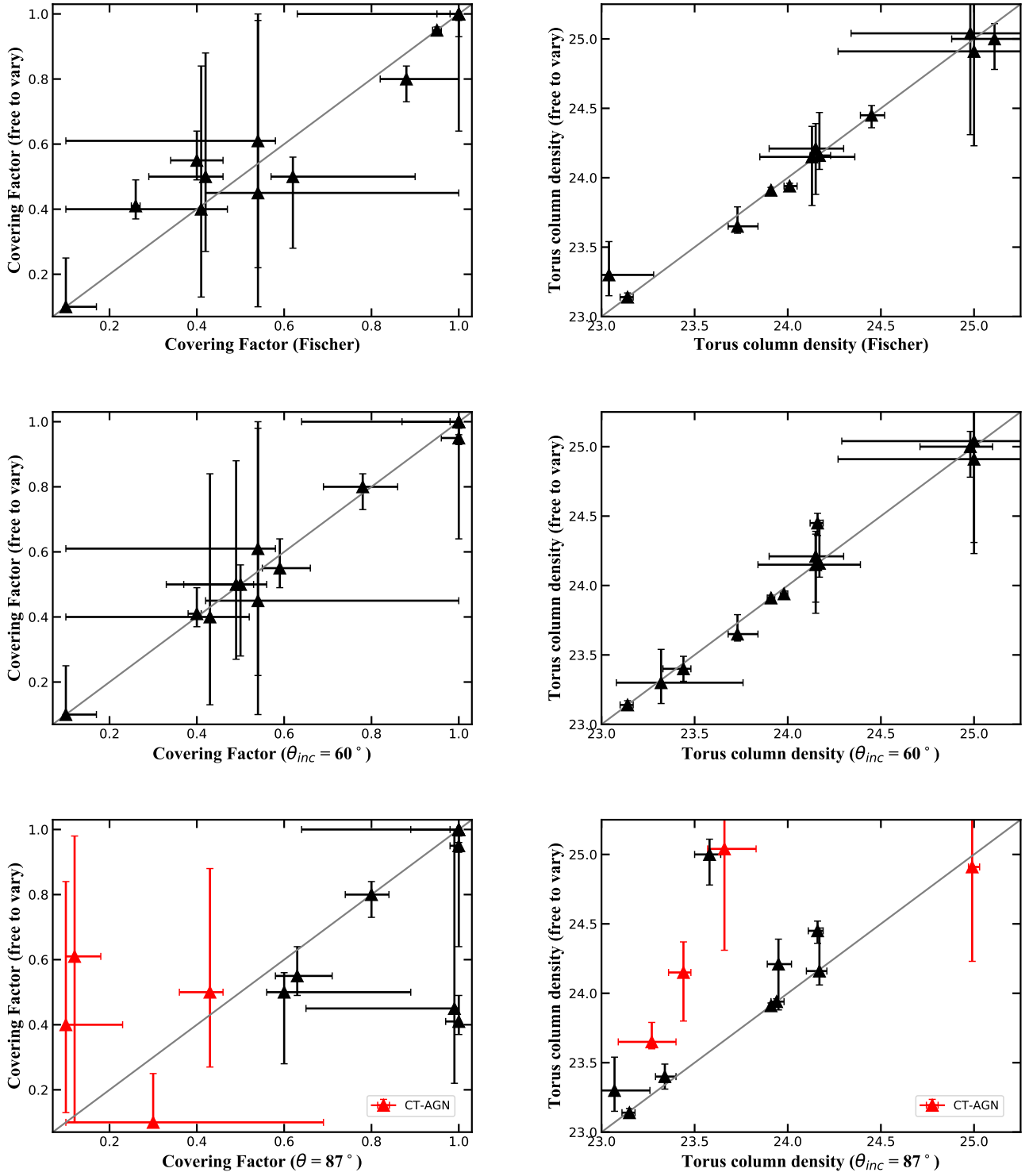


Figure 2. The figures from the left to right in different rows are the $c_{f,tor}$ and $N_{H,tor}$ best-fit values obtained when θ_{inc} is left free to vary with respect to those obtained when θ_{inc} is fixed at [OIII] measured values (first row), when θ_{inc} is fixed at $\theta_{inc} = 60^\circ$ (second row) and $\theta_{inc} = 87^\circ$ (third row), where gray solid line represents the 1:1 result. CT-AGNs are plotted in red in third row.

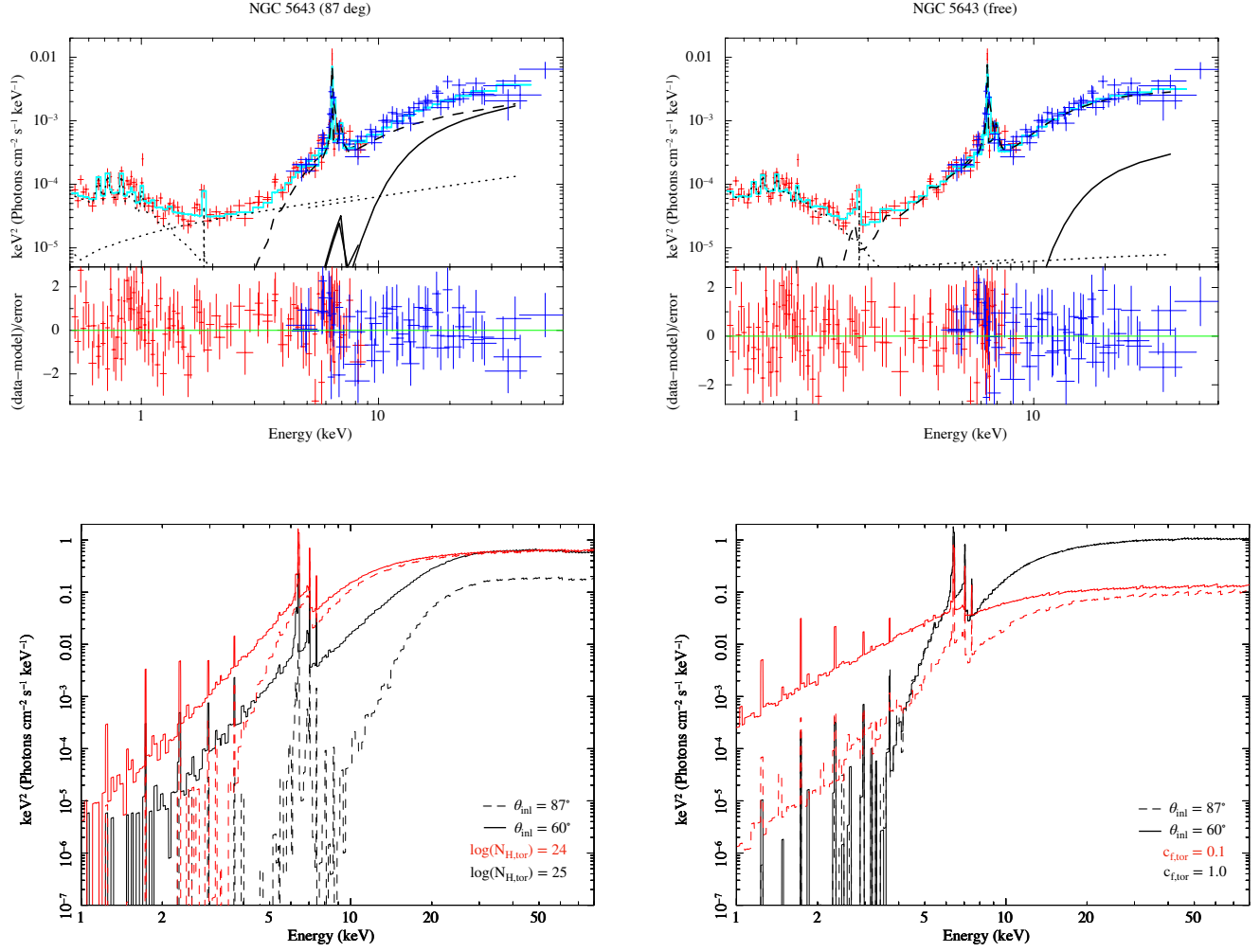


Figure 3. The figure is an illustrative example of how fixing the inclination angle at $\theta_{\text{inc}} = 87^\circ$ gives very different best-fit results compared to when the inclination angle is left free to vary in fitting the spectra and when the inclination angle at $\theta_{\text{inc}} = 60^\circ$. Top: unfolded spectra of NGC 5643 with inclination angle being fixed at $\theta_{\text{inc}} = 87^\circ$ and being left free to vary. The *NuSTAR* data are plotted in blue and the *XMM-Newton* data are plotted in red. The best-fit model prediction is plotted as cyan solid lines. The single components of the model are plotted in black with different line styles, i.e., the absorbed intrinsic continuum with solid lines, the reflection component with dashed lines, the scattered component, the *mekal* component and emission lines with dotted lines. Bottom: *borus02* model predictions of the reprocessed component when inclination angle are fixed at $\theta_{\text{inc}} = 87^\circ$ (dashed line) and $\theta_{\text{inc}} = 60^\circ$ (solid line). Left: the model predictions for $\log(N_{\text{H,tor}}) = 24$ (red) and $\log(N_{\text{H,tor}}) = 25$ (black): a photon index with $\Gamma = 1.8$ and torus covering factor with $c_{f,\text{Tor}} = 0.6$ are assumed. Right: the model predictions for $c_{f,\text{Tor}} = 0.1$ (red) and $c_{f,\text{Tor}} = 1.0$ (black): a photon index with $\Gamma = 1.8$ and torus column density with $\log(N_{\text{H,tor}}) = 24$ are assumed.

processed component when the inclination angles are $\theta_{\text{inc}} = 60^\circ$ and $\theta_{\text{inc}} = 87^\circ$ and the torus column densities are $\log(N_{\text{H,tor,free}}) = 24$ and $\log(N_{\text{H,tor,free}}) = 25$. When the inclination moves from $\theta_{\text{inc}} = 60^\circ$ to $\theta_{\text{inc}} = 87^\circ$, the spectra are suppressed significantly and nonlinearly: the spectra with energy below ~ 20 keV are much affected. Therefore, the torus column density decreases to compensate this reduction, which better describes the energy between ~ 5 keV to ~ 20 keV. The discrepancy of the spectra in other energy bands thus needs other components to make up, e.g., the line-of-sight component contributes more to the spectra at energy > 20 keV by decreasing the line-of-sight column density and the scattering component dominates the spectra at energy below ~ 4 keV by artificially increasing f_s .

The discrepancy of $c_{\text{f,tor}}$, however, is more complex due to the fact that the reprocessed component is energy dependent with respect to $c_{\text{f,tor}}$, as plotted in the bottom right panel of Figure 3, which plots the spectra of reprocessed component with different combinations of θ_{inc} and $c_{\text{f,tor}}$. For more information about the reprocessed component of the `borus02` model, we plot the `borus02` model predictions with varying different parameters in Appendix A.

Fixing the inclination angle at $\theta_{\text{inc}} = 87^\circ$ puts the strongest constraint on the parameters, e.g., $N_{\text{H,l.o.s}}$ and $N_{\text{H,tor}}$, among other cases. Such a result is caused by the fact that by fixing the inclination angle at $\theta_{\text{inc}} = 87^\circ$, the change in other parameters will lead to large variation on the spectrum: for example, in figure 3, we find that the spectral shape variation is much larger for $\theta_{\text{inc}} = 87^\circ$ than for $\theta_{\text{inc}} = 60^\circ$ when $N_{\text{H,tor}}$ varies, thus, the uncertainty of $N_{\text{H,tor}}$ is much less when using $\theta_{\text{inc}} = 87^\circ$ than using $\theta_{\text{inc}} = 60^\circ$. However, the $c_{\text{f,tor}}$ -related spectral variation is energy dependent in both $\theta_{\text{inc}} = 87^\circ$ and $\theta_{\text{inc}} = 60^\circ$ cases, therefore the average uncertainties of $c_{\text{f,tor}}$ are similar in the two cases.

4.4. Distribution of the obscuring material

In Section 4.1, Section 4.2 and Section 4.3, we discussed how varying the inclination angle affects the measurement of the other spectral parameters of AGNs. Thanks to the flexible and powerful `borus02` model, we could explore a larger parameter space in modeling the spectrum of AGN, e.g., we could now directly measure the average column density and the covering factor of the obscuring torus in AGN. Therefore, in this section, we focus on the correlations among different physical and geometrical properties of the sources in our sample.

A corner plot is drawn in Fig. 4 to explore the correlation among different parameters, i.e., line-of-sight column density, $\log(N_{\text{H,l.o.s}})$, torus column density, $\log(N_{\text{H,tor}})$, torus covering factor, c_{f} , 2–10 keV intrinsic luminosity, $L_{\text{int,2-10}}$, and Eddington ratio⁹, λ_{Edd} . Kendall's tau tests are performed for each pair of parameters and are labeled in each subplot. The best-fit values used are obtained when the inclination angle is left free

⁹ The Eddington ratio is calculated by $\lambda_{\text{Edd}} \equiv L_{\text{bol}}/L_{\text{Edd}}$, where L_{bol} is the bolometric luminosity. Bolometric luminosity is calculated by $L_{\text{bol}} = \kappa L_{\text{int,2-10}}$, assuming a bolometric correction $\kappa = 20$ (Vasudevan et al. 2010). Eddington luminosity is calculated as $L_{\text{Edd}} = 4\pi G M_{\text{BH}} m_p c / \sigma_T$, where M_{BH} is the mass of SMBH and m_p is the mass of proton.

to vary in fitting the spectra. We also plot the inclination angle as functions of other properties in Appendix B to explore the correlation between the inclination angle and other properties of the sources.

- We find no correlation between the measured AGN inclination angle and the other physical and geometrical properties of the AGN as show in Fig. 8. Such a result is reasonable since the sources are randomly observed and the properties of the sources should not be related to the angle at which they are observed.
- We find no correlations between intrinsic luminosity and torus column density ($p = 0.68$), torus column density and line-of-sight column density ($p = 0.31$), intrinsic luminosity and line-of-sight column density ($p = 0.25$), Eddington ratio and 2–10 keV intrinsic luminosity ($p = 0.25$) and torus covering factor and torus column density ($p = 0.22$).
- We find a correlation with confidence level $\sim 2.9 \sigma$ between the line-of-sight column density and Eddington ratio ($p = 0.004$), i.e., as the line-of-sight column density increases, the Eddington ratio also increases. We also find an inverse correlation with confidence level $\sim 2 \sigma$ between the line-of-sight column density and torus covering factor ($p = 0.05$), i.e., as the line-of-sight column density increases, the torus covering factor decreases. However, such trends are less evident if we exclude the sources which have been observed to be variable due to the shift of line-of-sight column density, which are marked as gray in Figure 4 from our analysis: the p values become $p = 0.07$ for line-of-sight column density and Eddington ratio and $p = 0.22$ for line-of-sight column density and torus covering factor. Therefore, we are not able confirm the correlation found between line-of-sight column density and Eddington ratio and the inverse correlation between the line-of-sight column density and torus covering factor.
- We find a correlation with confidence level $\sim 2.6 \sigma$ between the 2–10 keV intrinsic luminosity and the torus covering factor ($p = 0.01$), i.e., as the intrinsic luminosity increases, the torus covering factor decreases. Such a trend has been reported in many previous works with larger samples and higher statistical accuracy in different redshift range (e.g., Lawrence & Elvis 1982; Hasinger, G. 2008; Ueda et al. 2014). The covering factor of the torus in these works is derived from the X-ray hardness ratio or the fraction of the obscured Compton thin sources ($22 \leq \log(N_{\text{H}}) \leq 24$) in these works. Similar trend has also been found by Baloković (2017), which measured the individual torus covering factors and their intrinsic luminosities as in this work.
- We find an inverse correlation with confidence level $\sim 3 \sigma$ between the Eddington ratio and torus covering factor ($p = 0.003$), i.e., as the Eddington ratio of the AGN increases, the covering factor of the obscuring torus decreases. We also find a correlation

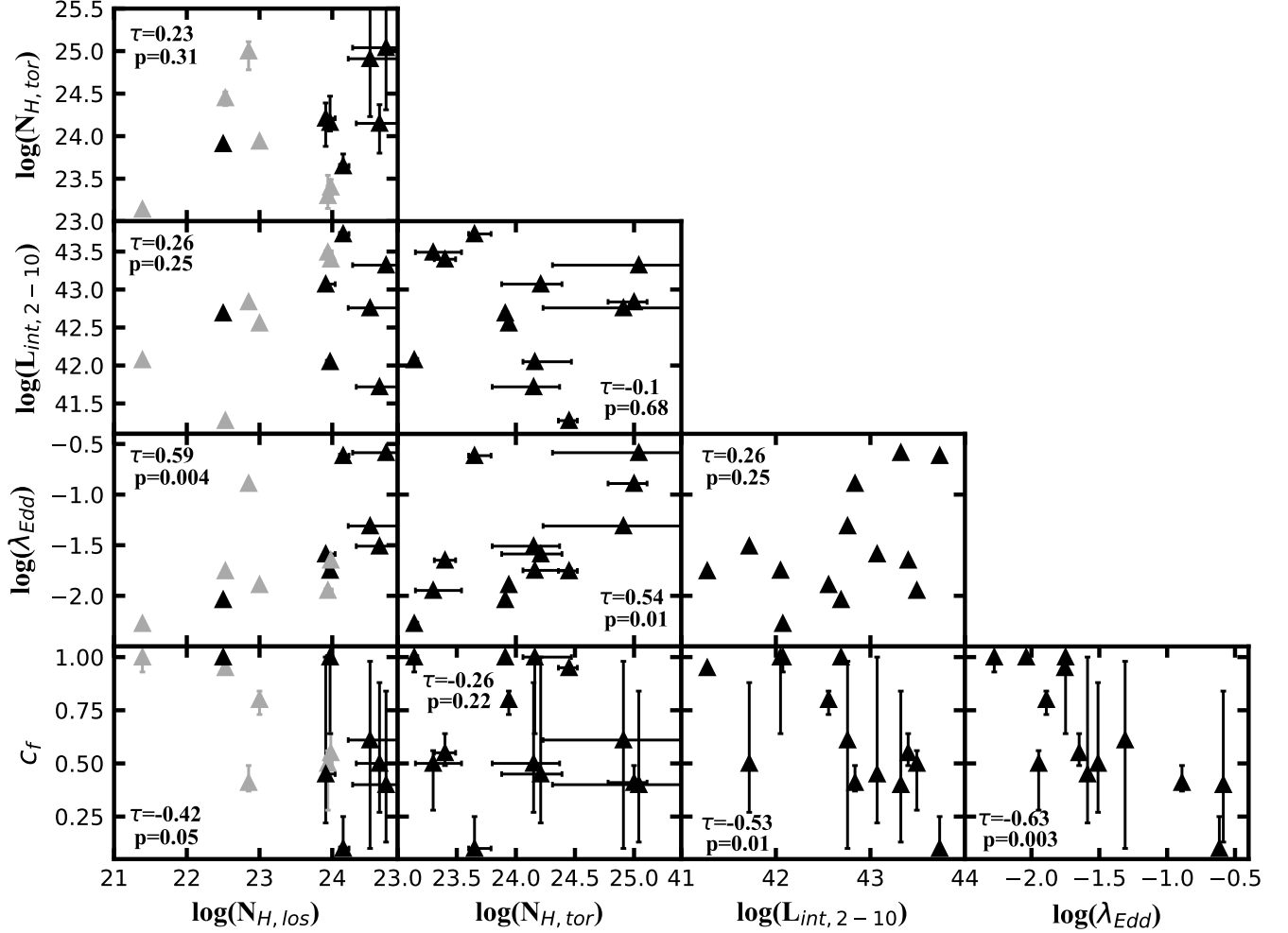


Figure 4. Best-fit results of different parameters, i.e., line-of-sight column density, $N_{\text{H},\text{los}}$, torus column density, $N_{\text{H},\text{tor}}$, torus covering factor, c_f , 2–10 keV intrinsic luminosity, $L_{\text{int},2-10}$ and Eddington ratio, λ_{Edd} , as a function of each other. Sources with known line-of-sight column density variability are plotted in gray. The tau values and p values in the Kendalls tau test are computed for each pair of parameters and are also labeled in each sub-plot.

with confidence level $\sim 2.6\sigma$ between the Eddington ratio and torus column density ($p = 0.01$), i.e., as the Eddington ratio of the AGN increases, the average column density of the obscuring torus decreases. Such results are in good agreement with those reported in Ricci et al. (2017), who found that the torus covering factor and the torus average column density strongly depends on the Eddington ratio of the AGN using a larger BAT selected sample of 392 AGNs. The dependence of torus covering factor and torus average column density on the Eddington ratio can be explained assuming that the distribution of the circumnuclear material around the SMBH is mainly regulated by the radiative feedback: as the accretion rate increases, the radiation pressure from the accretion disk blows the less dense ($\log(N_{\text{H}}) \leq 24$) materials away and leaves only the CT materials, thus decreasing the torus covering factor and increasing the torus average column density (Fabian et al. 2006, 2009; Ricci et al. 2017). We point out that in Ricci et al. (2017), the covering factors are indirectly measured, using as the fraction of obscured

($22 \leq \log(N_{\text{H}})$) AGNs with respect to all AGNs with $20 \leq \log(N_{\text{H}})$ in their sample. To better visualize the above correlations, we display the best-fit torus covering factors as a function of their measured Eddington ratio and the best-fit torus column density as a function of their measured Eddington ratio separately in Fig. 5. To compare with the results obtained in Ricci et al. (2017), we rebin our results in plotting the torus covering factors as a function of Eddington ratio. We find that our average torus covering factor are in good agreement with what Ricci et al. (2017) obtain, especially at large Eddington ratio.

The fact that no correlation is found between 2–10 keV intrinsic luminosity and torus average column density, together with the correlations found between torus covering factor and torus average column density with respect to the Eddington ratio, suggests that the distribution of the obscuring materials surrounding the SMBH of the AGNs in our sample is mainly regulated by the Eddington ratio rather than the intrinsic luminosity, which is in agreement with what is found in Ricci et al. (2017). Nevertheless, the exploration of the distribution of the

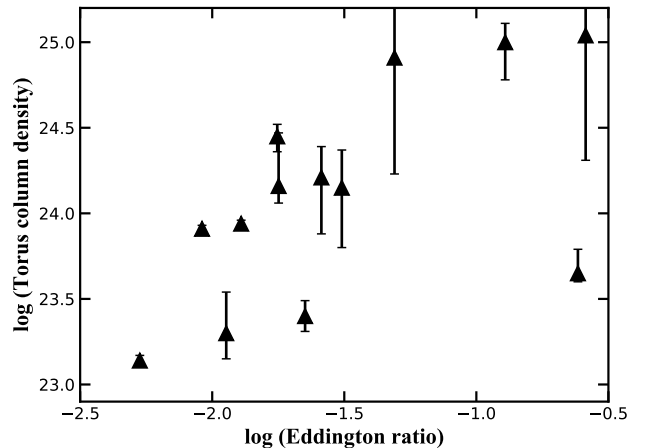
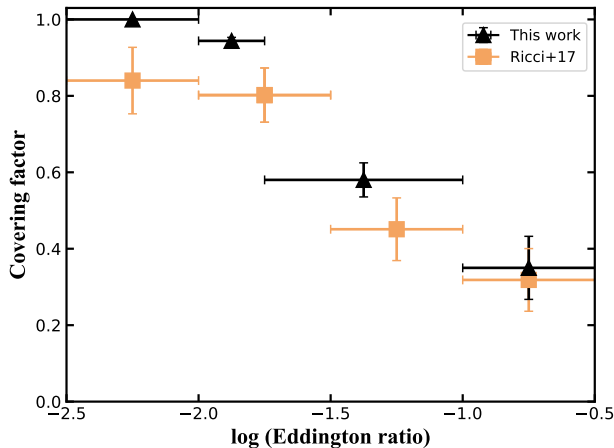


Figure 5. Left: torus covering factors as a function of the Eddington ratio of the 13 sources, which are rebinned to compare with the torus covering factor and Eddington ratio relationship measured in Ricci et al. (2017) (orange squares). The results are rebinned to make sure that each bin has similar number of sources. Right: torus column densities as a function of Eddington ratio of the 13 sources.

materials in the obscuring torus in AGN needs to be further studied in a larger unbiased sample with high-quality spectra.

4.5. Geometrical properties of torus and NLR

According to the unified model, the dusty torus obscures the radiation from the center engine of the AGN, and is therefore thought to form the biconical shape of the NLR or the ionization cone (Malkan et al. 1998). Fischer et al. (2013) report the opening angle of the outer edge of the NLR obtained by modeling the kinematics of the sources’ NLR observed with the *Hubble Space Telescope* (HST) and the Space Telescope Imaging Spectrograph (STIS). In this section, we explore the relation between the geometrical properties of the AGNs in our sample measured in optical and measured in X-ray.

In Figure 6, we plot the covering factor of the region excluding the NLR measured in optical, i.e., $1 - c_{f,\text{NLR}}$, as a function of the covering factor of the torus measured in X-ray, i.e., $c_{f,\text{Tor}}$. We find that: 1. there is no correlation between $c_{f,\text{tor}}$ and $1 - c_{f,\text{NLR}}$ ($\tau = 0.18$ and $p = 0.42$); 2. while $c_{f,\text{Tor}}$ span all values from 0.1 to 1, $c_{f,\text{NLR}}$ does not (i.e., $c_{f,\text{NLR}} < 0.5$). However, our results may be biased by the fact that: *borus02* assumes a uniformly distributed obscuring material scenario, therefore the $c_{f,\text{Tor}}$ measured in *borus02* is the effective fraction of the sky that is covered by the obscuring material, which thus gives the lower limit of the realistic clumpy $c_{f,\text{Tor}}$; the optical emission associated with the NLR measured by Fischer et al. (2013) may contain the emission from star formation process, which might lead to inaccurate measurement of the geometry of the NLR. Therefore, further studies with larger sample of AGNs with multi-wavelength datasets are needed to understand the geometrical properties of different components of the AGN.

5. CONCLUSION

We performed a broadband X-ray spectral analysis on a sample of AGNs selected from Fischer et al. (2013) with [OIII] measured inclination angle, using high-quality

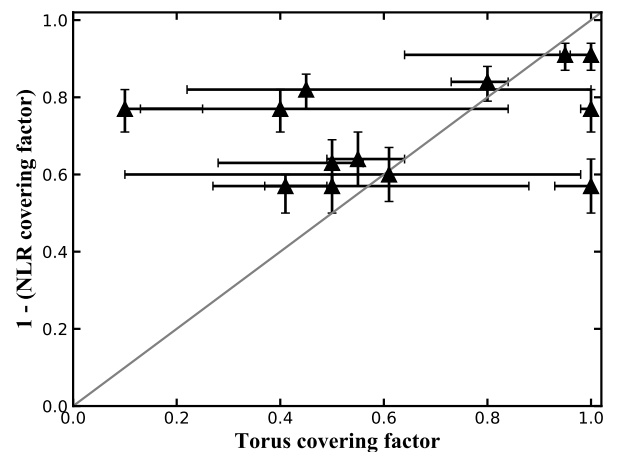


Figure 6. Relationship between the covering factor of the region excluding the NLR, i.e., $1 - c_{f,\text{NLR}}$, with respect to the covering factor of the torus, i.e., $c_{f,\text{Tor}}$. The gray solid line represents the 1:1 result.

NuSTAR, *XMM-Newton* and *Chandra* archival data. To model the spectra, we utilized the recently published self-consistent *borus02* model, which is effective in characterizing the physical and geometrical properties of the obscuring materials near the SMBH. The main findings of this work are reported as follows.

- The best-fit values of the spectral parameters obtained when the sources are fitted with the inclination angle being fixed at the [OIII] measured values are similar to those obtained when inclination angle is left free to vary. Fixing the inclination angle at $\theta_{\text{inc}} = 60^\circ$ also gives similar spectral fit results, but incorrect fit results may be obtained for some CT sources out of our sample; fixing the inclination angle at $\theta_{\text{inc}} = 87^\circ$ leads to significant different measurements of the torus covering factor and the torus column density even for CT-AGNs, but gives the best constraints on different parameters.

- In AGN X-ray spectral analysis, one should always let the inclination angle free to vary. If one intends to better constrain the properties of sources when fitting low quality X-ray spectra (i.e., ≤ 300 d.o.f), one should fit the spectra by letting θ_{inc} free to vary at first, then fix θ_{inc} at some reasonable values, e.g., $\theta_{\text{inc}} = 60^\circ$ or [OIII] measured values. Comparing the best-fit results of the two methods: only when the best-fit values of all parameters fitted when fixing the θ_{inc} are in good agreement with those obtained when letting θ_{inc} free to vary in fitting the spectra, one could fix θ_{inc} at those values, otherwise, fixing θ_{inc} at some preferred values should always be avoided and θ_{inc} should be left free to vary in fitting these spectra.
- The properties of AGNs in our sample are not dependent on the direction at which they are observed, i.e., the inclination angle.
- We confirm a strong inverse correlation between the torus covering factor and the Eddington ratio, and a correlation between the torus average column density and the Eddington ratio measured in the sources of our sample, which is in good agreement with the radiative feedback model. We also find an inverse correlation between the torus covering factor and the 2–10 keV intrinsic luminosity, which has also been measured in previous works. However, we do not find any correlation between the torus average column density and the 2–10 keV intrinsic luminosity, suggesting that the distribution of the materials in the obscuring torus are regulated by the Eddington ratio rather than the intrinsic luminosity.
- We found no geometrical correlation between the two components of AGN, i.e., obscuring torus and NLR: the torus covering factors span all values, while the covering factors of NLR do not. The ability to robustly measure the covering factor of the torus in the X-ray band is currently limited by the data quality, sample size, and the lack of sufficiently realistic spectral model, which we expect to improve in future work. However, this result already suggests that AGN geometry might be more complex than what is assumed in the simplistic unified model of AGN.

X.Z. thanks the anonymous referee for their detailed and useful comments, which helped significantly improve the paper. X.Z., S.M., and M.A. acknowledge NASA funding under contract 80NSSC17K0635 and 80NSSC19K0531. M.B. acknowledges support from the Black Hole Initiative at Harvard University, which is funded in part by the Gordon and Betty Moore Foundation (grant GBMF8273) and in part by the John Templeton Foundation. *NuSTAR* is a project led by the California Institute of Technology (Caltech), managed by the Jet Propulsion Laboratory (JPL), and funded by the National Aeronautics and Space Administration (NASA). We thank the NuSTAR Operations, Software and Calibrations teams for support with these observations. This research has made use of the *NuSTAR* Data

Analysis Software (NuSTARDAS) jointly developed by the ASI Science Data Center (ASDC, Italy) and the California Institute of Technology (USA). This research has made use of data and/or software provided by the High Energy Astrophysics Science Archive Research Center (HEASARC), which is a service of the Astrophysics Science Division at NASA/GSFC and the High Energy Astrophysics Division of the Smithsonian Astrophysical Observatory. This work is based on observations obtained with *XMM-Newton*, an ESA science mission with instruments and contributions directly funded by ESA Member States and NASA.

REFERENCES

- Alexander, D. M., Bauer, F. E., Brandt, W. N., et al. 2003, *The Astronomical Journal*, 126, 539
- Almeida, C. R., Levenson, N. A., Espinosa, J. M. R., et al. 2009, *The Astrophysical Journal*, 702, 1127
- Almeida, C. R. & Ricci, C. 2017, *Nature Astronomy*, 1, 679
- Ananna, T. T., Treister, E., Urry, C. M., et al. 2019, *The Astrophysical Journal*, 871, 240
- Anders, E. & Grevesse, N. 1989, *Geochimica et Cosmochimica Acta*, 53, 197
- Annuar, A., Gandhi, P., Alexander, D. M., et al. 2015, *The Astrophysical Journal*, 815, 36
- Antonucci, R. 1993, *Annu. Rev. Astron. Astrophys.*, 31, 473
- Arévalo, P., Bauer, F. E., Puccetti, S., et al. 2014, *The Astrophysical Journal*, 791, 81
- Arnaud, K. A. 1996, *Astronomical Data Analysis Software and Systems V*, 101, 17
- Baloković, M. 2017, PhD thesis, California Institute of Technology
- Baloković, M., Brightman, M., Harrison, F. A., et al. 2018, *The Astrophysical Journal*, 854, 42
- Baloković, M., Comastri, A., Harrison, F. A., et al. 2014, *The Astrophysical Journal*, 794, 111
- Barthelmy, S. D., Barbier, L. M., Cummings, J. R., et al. 2005, *Space Science Reviews*, 120, 143
- Bauer, F. E., Arévalo, P., Walton, D. J., et al. 2015, *The Astrophysical Journal*, 812, 116
- Bauer, F. E., Brandt, W. N., Sambruna, R. M., et al. 2001, *The Astronomical Journal*, 122, 182
- Beifiori, A., Courteau, S., Corsini, E. M., & Zhu, Y. 2012, *Monthly Notices of the Royal Astronomical Society*, 419, 2497
- Beuchert, T., Markowitz, A. G., Dauser, T., et al. 2017, *A&A*, 603, A50
- Bianchi, S., Maiolino, R., & Risaliti, G. 2012, *Advances in Astronomy*, 2012, 17
- Boorman, P. G., Gandhi, P., Baloković, M., et al. 2018, *Monthly Notices of the Royal Astronomical Society*, 477, 3775
- Braitto, V., Ballo, L., Reeves, J. N., et al. 2012, *Monthly Notices of the Royal Astronomical Society*, 428, 2516
- Brightman, M., Baloković, M., Stern, D., et al. 2015, *The Astrophysical Journal*, 805, 41
- Brightman, M. & Nandra, K. 2011, *Monthly Notices of the Royal Astronomical Society*, 413, 1206
- De Marco, B., Adhikari, T. P., Ponti, G., et al. 2020, *A&A*, 634, A65
- Denney, K. D., Watson, L. C., Peterson, B. M., et al. 2009, *The Astrophysical Journal*, 702, 1353
- Fabian, A. C., Celotti, A., & Erlund, M. C. 2006, *Monthly Notices of the Royal Astronomical Society: Letters*, 373, L16
- Fabian, A. C., Iwasawa, K., Reynolds, C. S., & Young, A. J. 2000, *Publications of the Astronomical Society of the Pacific*, 112, 1145
- Fabian, A. C., Vasudevan, R. V., Mushotzky, R. F., Winter, L. M., & Reynolds, C. S. 2009, *Monthly Notices of the Royal Astronomical Society: Letters*, 394, L89
- Fischer, T. C., Crenshaw, D. M., Kraemer, S. B., & Schmitt, H. R. 2013, *The Astrophysical Journal Supplement Series*, 209, 1
- Fruscione, A., McDowell, J. C., Allen, G. E., et al. 2006, *Proc. SPIE*, 6270, 62701V

- Fürst, F., Müller, C., Madsen, K. K., et al. 2016, *The Astrophysical Journal*, 819, 150
- Furui, S., Fukazawa, Y., Odaka, H., et al. 2016, *The Astrophysical Journal*, 818, 164
- Gandhi, P., Annuar, A., Lansbury, G. B., et al. 2017, *Monthly Notices of the Royal Astronomical Society*, 467, 4606
- Gandhi, P. & Fabian, A. C. 2003, *Monthly Notices of the Royal Astronomical Society*, 339, 1095
- Gandhi, P., Lansbury, G. B., Alexander, D. M., et al. 2014, *The Astrophysical Journal*, 792, 117
- Georgantopoulos, I., Comastri, A., Vignali, C., et al. 2013, *A&A*, 555, A43
- Ghisellini, G., Haardt, F., & Matt, G. 1994, *Monthly Notices of the Royal Astronomical Society*, 267, 743
- Gilli, R., Comastri, A., & Hasinger, G. 2007, *A&A*, 463, 79
- Goulding, A. D., Alexander, D. M., Lehmer, B. D., & Mullaney, J. R. 2010, *Monthly Notices of the Royal Astronomical Society*, 406, 597
- Harrison, F. A., Craig, W. W., Christensen, F. E., et al. 2013, *The Astrophysical Journal*, 770, 103
- Hasinger, G. 2008, *A&A*, 490, 905
- Heckman, T. M. & Best, P. N. 2014, *Annual Review of Astronomy and Astrophysics*, 52, 589
- Hickox, R. C. & Alexander, D. M. 2018, *Annual Review of Astronomy and Astrophysics*, 56, 625
- Ikeda, S., Awaki, H., & Terashima, Y. 2009, *The Astrophysical Journal*, 692, 608
- Jansen, F., Lumb, D., Altieri, B., et al. 2001, *A&A*, 365, L1
- Kalberla, P. M. W., Burton, W. B., Hartmann, Dap, et al. 2005, *A&A*, 440, 775
- Kammoun, E. S., Miller, J. M., Zoghbi, A., et al. 2019, *The Astrophysical Journal*, 877, 102
- Kawamuro, T., Ueda, Y., Tazaki, F., & Terashima, Y. 2013, *The Astrophysical Journal*, 770, 157
- Kormendy, J. & Ho, L. C. 2013, *Annual Review of Astronomy and Astrophysics*, 51, 511
- Koss, M. J., Assef, R., Baloković, M., et al. 2016, *The Astrophysical Journal*, 825, 85
- Koss, M. J., Romero-Cañizales, C., Baronchelli, L., et al. 2015, *The Astrophysical Journal*, 807, 149
- Krolik, J. H. & Begelman, M. C. 1988, *Astrophysical Journal*, 329, 702
- Krolik, J. H., Madau, P., & Zycki, P. T. 1994, *ApJ*, 420, L57
- La Caria, M.-M., Vignali, C., Lanzuisi, G., Gruppioni, C., & Pozzi, F. 2019, *Monthly Notices of the Royal Astronomical Society*, 487, 1662
- LaMassa, S. M., Yaqoob, T., Ptak, A. F., et al. 2014, *The Astrophysical Journal*, 787, 61
- Lawrence, A. & Elvis, M. 1982, *ApJ*, 256, 410
- Leahy, D. A. & Creighton, J. 1993, *Monthly Notices of the Royal Astronomical Society*, 263, 314
- Li, J., Xue, Y., Sun, M., et al. 2019, *The Astrophysical Journal*, 877, 5
- Liu, Y. & Li, X. 2014, *The Astrophysical Journal*, 787, 52
- Malkan, M. A., Gorjian, V., & Tam, R. 1998, *The Astrophysical Journal Supplement Series*, 117, 25
- Mao, J., Mehdipour, M., Kaastra, J. S., et al. 2019, *A&A*, 621, A99
- Marchesi, S., Ajello, M., Marcotulli, L., et al. 2018, *The Astrophysical Journal*, 854, 49
- Marchesi, S., Ajello, M., Zhao, X., et al. 2019, *The Astrophysical Journal*, 872, 8
- Marchesi, S., Tremblay, L., Ajello, M., et al. 2017, *The Astrophysical Journal*, 848, 53
- Marinucci, A., Matt, G., Kara, E., et al. 2014, *Monthly Notices of the Royal Astronomical Society*, 440, 2347
- Marinucci, A., Risaliti, G., Wang, J., et al. 2013, *Monthly Notices of the Royal Astronomical Society*, 429, 2581
- Markowitz, A. G., Krumpke, M., & Nikutta, R. 2014, *Monthly Notices of the Royal Astronomical Society*, 439, 1403
- Masini, A., Comastri, A., Hickox, R. C., et al. 2019, *The Astrophysical Journal*, 882, 83
- Matt, G. 2002, *Monthly Notices of the Royal Astronomical Society*, 337, 147
- Matt, G. & Fabian, A. C. 1994, *Monthly Notices of the Royal Astronomical Society*, 267, 187
- Mehdipour, M., Kaastra, J. S., Kriss, G. A., et al. 2017, *A&A*, 607, A28
- Merritt, D. & Ferrarese, L. 2001, *Monthly Notices of the Royal Astronomical Society*, 320, L30
- Mewe, R., Gronenschild, E. H. B. M., & van den Oord, G. H. J. 1985, *A&AS*, 62, 197
- Mizumoto, M. & Ebisawa, K. 2016, *Monthly Notices of the Royal Astronomical Society*, 466, 3259
- Murphy, K. D. & Yaqoob, T. 2009, *Monthly Notices of the Royal Astronomical Society*, 397, 1549
- Nandra, K. 2001, *Advances in Space Research*, 28, 295
- Nelson, C. H. & Whittle, M. 1995, *ApJS*, 99, 67
- Neškova, M., Sirocky, M. M., Ivezić, Ž., & Elitzur, M. 2008, *The Astrophysical Journal*, 685, 147
- Netzer, H. 2015, *Annual Review of Astronomy and Astrophysics*, 53, 365
- Nicastro, F., Martocchia, A., & Matt, G. 2003, *The Astrophysical Journal*, 589, L13
- Nikolajuk, M., Czerny, B., & Gurynowicz, P. 2009, *Monthly Notices of the Royal Astronomical Society*, 394, 2141
- Noguchi, K., Terashima, Y., Ishino, Y., et al. 2010, *The Astrophysical Journal*, 711, 144
- Onken, C. A. & Peterson, B. M. 2002, *The Astrophysical Journal*, 572, 746
- Onken, C. A., Peterson, B. M., Dietrich, M., Robinson, A., & Salamanca, I. M. 2003, *The Astrophysical Journal*, 585, 121
- Onken, C. A., Valluri, M., Peterson, B. M., et al. 2007, *The Astrophysical Journal*, 670, 105
- Paltani, S. & Ricci, C. 2017, *A&A*, 607, A31
- Puccetti, S., Comastri, A., Fiore, F., et al. 2014, *The Astrophysical Journal*, 793, 26
- Reynolds, C. S. 1999, in *Astronomical Society of the Pacific Conference Series*, Vol. 161, *High Energy Processes in Accreting Black Holes*, ed. J. Poutanen & R. Svensson, 178
- Reynolds, C. S. & Nowak, M. A. 2003, *Physics Reports*, 377, 389
- Ricci, C., Bauer, F. E., Treister, E., et al. 2016, *The Astrophysical Journal*, 819, 4
- Ricci, C., Trakhtenbrot, B., Koss, M. J., et al. 2017, *Nature*, 549, 488 EP
- Ricci, C., Ueda, Y., Paltani, S., et al. 2014, *Monthly Notices of the Royal Astronomical Society*, 441, 3622
- Risaliti, G., Elvis, M., Fabbiano, G., Baldi, A., & Zezas, A. 2005, *The Astrophysical Journal*, 623, L93
- Risaliti, G., Elvis, M., & Nicastro, F. 2002, *The Astrophysical Journal*, 571, 234
- Shu, X. W., Yaqoob, T., & Wang, J. X. 2010, *The Astrophysical Journal Supplement Series*, 187, 581
- Strüder, L., Briel, U., Dennerl, K., et al. 2001, *A&A*, 365, L18
- Sun, S., Guainazzi, M., Ni, Q., et al. 2018, *Monthly Notices of the Royal Astronomical Society*, 478, 1900
- Tanimoto, A., Ueda, Y., Odaka, H., et al. 2019, *The Astrophysical Journal*, 877, 95
- Treister, E., Urry, C. M., & Virani, S. 2009, *The Astrophysical Journal*, 696, 110
- Turner, M. J. L., Abbey, A., Arnaud, M., et al. 2001, *A&A*, 365, L27
- Turner, T. J., Miller, L., Reeves, J. N., & Braitto, V. 2017, *Monthly Notices of the Royal Astronomical Society*, 467, 3924
- Ueda, Y., Akiyama, M., Hasinger, G., Miyaji, T., & Watson, M. G. 2014, *The Astrophysical Journal*, 786, 104
- Urry, C. M. & Padovani, P. 1995, *Publications of the Astronomical Society of the Pacific*, 107, 803
- Ursini, F., Bassani, L., Panessa, F., et al. 2018, *Monthly Notices of the Royal Astronomical Society*, 474, 5684
- Ursini, F., Marinucci, A., Matt, G., et al. 2015, *Monthly Notices of the Royal Astronomical Society*, 452, 3266
- Ursini, F., Petrucci, P.-O., Matt, G., et al. 2016, *Monthly Notices of the Royal Astronomical Society*, 463, 382
- Vasudevan, R. V., Fabian, A. C., Gandhi, P., Winter, L. M., & Mushotzky, R. F. 2010, *Monthly Notices of the Royal Astronomical Society*, 402, 1081
- Verner, D., Ferland, G., Korista, K., & Yakovlev, D. 1996, *Astrophysical Journal*, 465, 487
- Walton, D. J., Nardini, E., Gallo, L. C., et al. 2019, *Monthly Notices of the Royal Astronomical Society*, 484, 2544
- Winkler, C., T. J.-L. Courvoisier, Di Cocco, G., et al. 2003, *A&A*, 411, L1

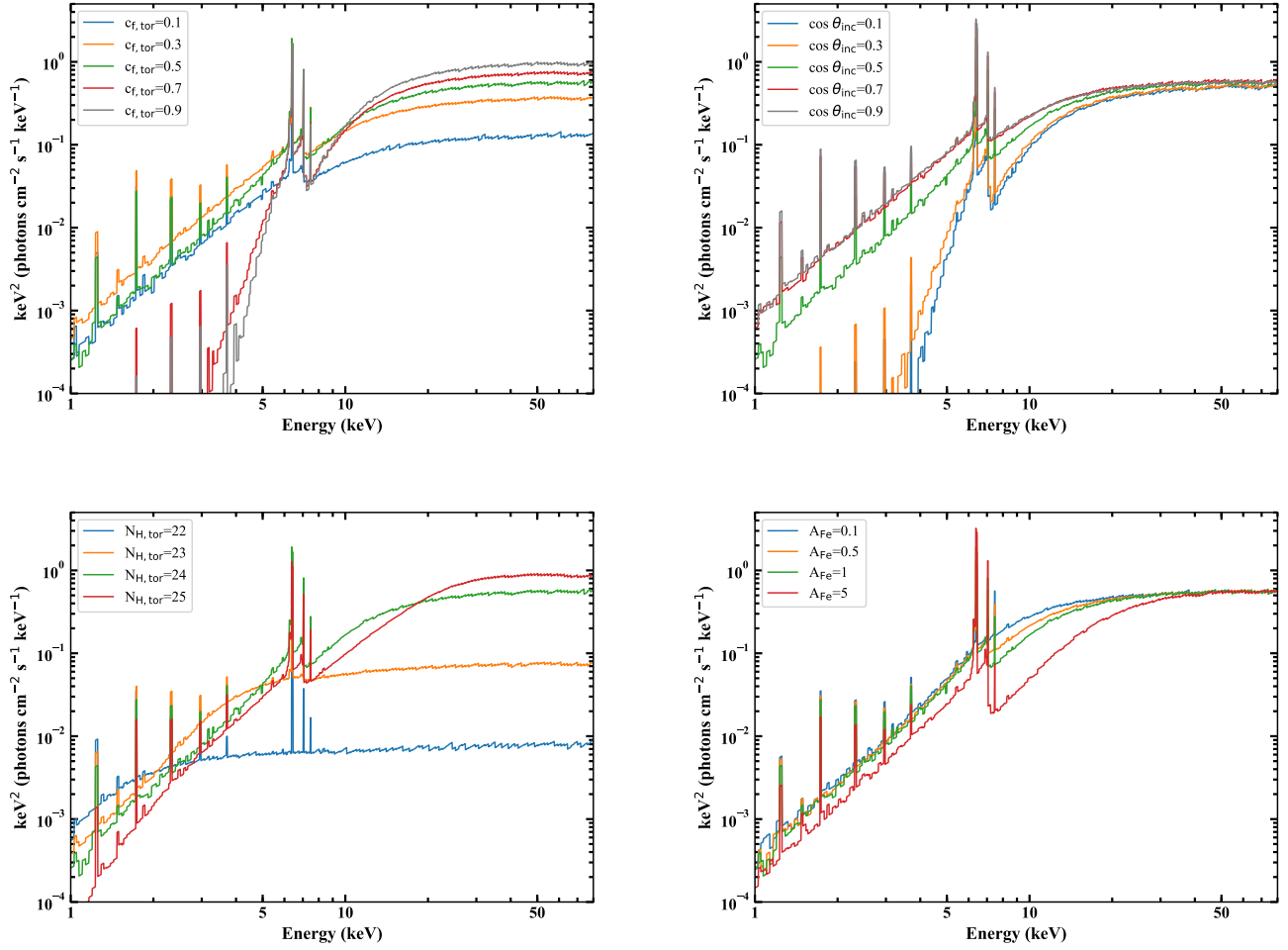


Figure 7. Top Left: Spectra of the `borus02` (Baloković et al. 2018) model prediction of the reprocessed component with varying $c_{f,tor}$, assuming $\cos(\theta_{inc}) = 0.5$, $\log(N_{H,tor}) = 24$ and $A_{Fe} = 1$. Top Right: Spectra of the `borus02` model prediction of the reprocessed component with varying θ_{inc} , assuming $c_{f,tor} = 0.5$, $\log(N_{H,tor}) = 24$ and $A_{Fe} = 1$. Bottom Left: Spectra of the `borus02` model prediction of the reprocessed component with varying $N_{H,tor}$, assuming $c_{f,tor} = 0.5$, $\cos(\theta_{inc}) = 0.5$ and $A_{Fe} = 1$. Bottom Right: Spectra of the `borus02` model prediction of the reprocessed component with varying A_{Fe} , assuming $c_{f,tor} = 0.5$, $\cos(\theta_{inc}) = 0.5$ and $\log(N_{H,tor}) = 24$. All spectra assumed a $\Gamma = 1.8$.

Woo, J.-H. & Urry, C. M. 2002, *The Astrophysical Journal*, 579, 530

Yaqoob, T. 2012, *Monthly Notices of the Royal Astronomical Society*, 423, 3360

Yaqoob, T. & Padmanabhan, U. 2004, *The Astrophysical Journal*, 604, 63

Yaqoob, T., Tatum, M. M., Scholtes, A., Gottlieb, A., & Turner, T. J. 2015, *Monthly Notices of the Royal Astronomical Society*, 454, 973

Zappacosta, L., Comastri, A., Civano, F., et al. 2018, *The Astrophysical Journal*, 854, 33

Zhao, X., Marchesi, S., & Ajello, M. 2019a, *The Astrophysical Journal*, 871, 182

Zhao, X., Marchesi, S., Ajello, M., et al. 2019b, *The Astrophysical Journal*, 870, 60

APPENDIX

A. `borus02` MODEL

We plot the spectra of `borus02` model prediction of the reprocessed component when varying different parameters, i.e., torus covering factor, $c_{f,tor}$, inclination angle, θ_{inc} , torus column density, $N_{H,tor}$, and relative iron abundance, A_{Fe} , in Figure 7.

B. DEPENDENCE OF THE PROPERTIES OF AGNS ON THEIR INCLINATIONS

We plot the best-fit inclination angle of the 13 sources in our sample as functions of their line-of-sight column density, torus covering factor, torus column density, Eddington ratio, 2–10 keV intrinsic luminosity in Figure 8. The tau and p values for each pair of properties are calculated and reported in each subplot. We find no correlation between the measured inclination angle of AGN and the other physical and geometrical properties of AGNs.

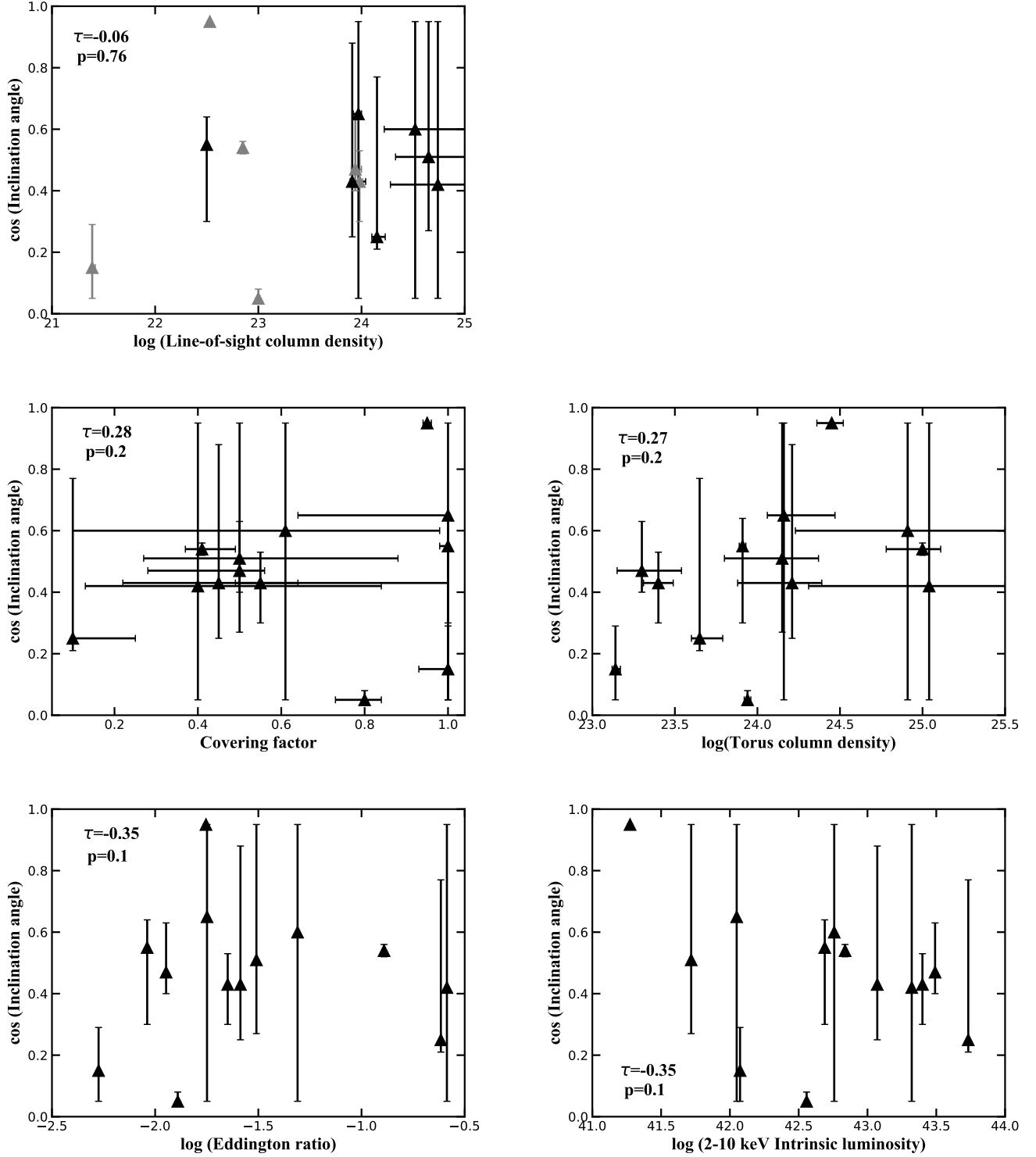


Figure 8. Best-fit inclination angle of the 13 sources in our sample as functions of their line-of-sight column density, torus covering factor, torus column density, Eddington ratio, 2–10 keV intrinsic luminosity in Figure 8. The tau and p values for each pair of properties are calculated and reported in each subplot. Sources which have been observed to be variable due to the variability of line-of-sight column density are marked as gray.

C. FITTING DETAILS AND SPECTRA OF 13 SOURCES

Fitting Details

Mrk 3: the cut-off energy E_{cut} of the source is found to be much less than the default 500 keV, thus we let E_{cut} free to vary in fitting the spectra of Mrk 3 and a $E_{\text{cut}} = 85_{-20}^{+55}$ keV is measured. The relative iron abundance is found to be less than the default value, thus the relative iron abundance is left free to vary in fitting the spectrum of Mrk 3 and an $A_{\text{Fe}} = 0.44_{-0.08}^{+0.14} A_{\text{Fe},\odot}$ is measured. The best-fit statistic of the scenario of letting θ_{inc} free to vary is $\chi^2/\text{degree of freedom (d.o.f)} = 1056/1073 \approx 0.98$. The best-fit photon index for Mrk 3 is $\Gamma = 1.48_{-u}^{+0.11}$, where u means the parameter cannot be constrained at 90% confidence level within the range of the parameter in the **borus02** model, which is [1.4–2.6] for Γ . The best-fit line-of-sight column density is $\log(N_{\text{H,l.o.s}}) = 23.94_{-0.04}^{+0.06}$ and the best-fit torus column density is $\log(N_{\text{H,tor}}) = 23.30_{-0.15}^{+0.24}$. The best-fit inclination angle is $\cos(\theta_{\text{inc}}) = 0.47_{-0.07}^{+0.16}$ and the best-fit covering factor is $c_{\text{f,tor}} = 0.50_{-0.22}^{+0.06}$.

Mrk 34: an energy range of 0.6 keV–78 keV rather than 0.5 keV–78 keV is used in fitting the spectrum of Mrk 34 since we found that the spectrum between 0.5 keV–2 keV cannot be fitted by a single **mekal** model, however, the spectrum between 0.6 keV–2 keV can be well fitted by a single **mekal** model. In addition, we added a number of unresolved Gaussian lines as needed to reach a good fit of Mrk 34. The best-fit statistic of Mrk 34 is $\chi^2/\text{d.o.f} = 74/82 \approx 0.90$. The best-fit photon index is $\Gamma = 1.45_{-u}^{+0.67}$. The best-fit line-of-sight column density is $\log(N_{\text{H,l.o.s}}) > 24.28$ and the best-fit torus column density is $\log(N_{\text{H,tor}}) = 25.04_{-0.73}^{+u}$, where the parameter range of $\log(N_{\text{H,tor}})$ in **borus02** table is [22.0–25.5]. The best-fit inclination angle is $\cos(\theta_{\text{inc}}) = 0.42_{-u}^{+u}$, suggesting that the inclination angle of Mrk 34 is unconstrained with current data. The best-fit covering factor of Mrk 34 is $c_{\text{f,tor}} = 0.40_{-0.27}^{+0.44}$.

Mrk 78: We adopted *NuSTAR* data from 4 keV to 78 keV since the *NuSTAR* data between 3–4 keV showed strong discrepancy with *XMM-Newton* and *Chandra* data. We found a strong emission line at ~ 8.265 keV in the spectrum, which belongs to the Ni K β emission line. Thus a gaussian line centered at $E_l = 8.265$ keV with zero width is added to better fit the spectrum. We compare the flux of the Ni K β emission line and Fe K α line: the measured flux of the Fe K α line of Mrk 78 is $F_{\text{lux,Fe K}\alpha} = 4.5 \times 10^{-15}$ erg cm $^{-2}$ s $^{-1}$ between 6.39 keV and 6.41 keV and the measured flux of the Ni K β line is $F_{\text{lux,Ni K}\beta} = 3.8 \times 10^{-15}$ erg cm $^{-2}$ s $^{-1}$ between 8.255 keV and 8.275 keV. Strong variability is also found between the *NuSTAR* observations and the three soft X-ray observations. The 2–10 keV flux of Mrk 78 observed in *NuSTAR* increased by $\sim 135\%$ with respect to the flux observed in *XMM-Newton*. We found that the variability observed in Mrk 78 is caused by both the variability of intrinsic emission and $N_{\text{H,l.o.s}}$ variability. The intrinsic emission of Mrk 78 measured using *NuSTAR* observation increased by $\sim 38\%$ with respect to the intrinsic emission measured using *XMM-Newton* observation and the $N_{\text{H,l.o.s}}$ observed in *NuSTAR* decreased by 49% with respect to the $N_{\text{H,l.o.s}}$ observed in *XMM-Newton*, i.e., $\log(N_{\text{H,l.o.s},\text{NuS}}) = 23.62_{-0.08}^{+0.08}$ from $\log(N_{\text{H,l.o.s},\text{XMM}}) = 23.91_{-0.02}^{+0.13}$. The best-fit statistic of Mrk 78 is $\chi^2/\text{d.o.f} = 276/271 \approx 1.02$. The best-fit photon index of Mrk 78 is $\Gamma = 1.40_{-u}^{+0.21}$. The best-fit torus column density is $\log(N_{\text{H,tor}}) = 24.21_{-0.33}^{+0.18}$. The best-fit inclination angle is $\cos(\theta_{\text{inc}}) = 0.43_{-0.18}^{+0.45}$ and the best-fit covering factor is found to be $c_{\text{f,tor}} > 0.22$.

Mrk 573: an energy range of 0.3 keV–78 keV rather than 0.5 keV–78 keV is used in fitting the spectrum of Mrk 573 because we found the spectrum of Mrk 573 between 0.5 keV–2 keV can not be fitted by a single **mekal** model. Although the spectrum between 0.8 keV–2 keV can be fitted by a single **mekal** model, to exploit the high-quality *XMM-Newton* data below 0.8 keV, which provide ~ 2600 more counts (the total counts in the spectra between 0.8 keV–78 keV are ~ 2400 cts), we fit the spectra of Mrk 573 in the 0.3 keV–78 keV energy band and add another **mekal** in our modeling. The best-fit statistic of Mrk 573 is $\chi^2/\text{d.o.f} = 152/194 \approx 0.78$. The best-fit photon index is $\Gamma = 2.35_{-0.65}^{+u}$. The best-fit line-of-sight column density is $\log(N_{\text{H,l.o.s}}) > 24.22$ and the best-fit average torus column density is $\log(N_{\text{H,tor}}) > 24.23$. The best-fit inclination angle is $\cos(\theta_{\text{inc}}) = 0.60_{-u}^{+u}$ and the best-fit torus covering factor is $c_{\text{f,tor}} < 0.98$, suggesting that we are unable to constrain both the inclination and the torus covering factor of Mrk 573.

Mrk 1066: the cut-off energy E_{cut} of Mrk 1066 is found to be $E_{\text{cut}} < 28$ keV. The relative iron abundance is found to be $A_{\text{Fe}} = 3.2_{-1.0}^{+0.7} A_{\text{Fe},\odot}$. In addition, we added a number of unresolved Gaussian lines as needed to reach a good fit of Mrk 1066. The best-fit statistic of Mrk 1066 is $\chi^2/\text{d.o.f} = 142/147 \approx 0.97$. The best-fit photon index is $\Gamma = 1.52_{-u}^{+0.02}$. The best-fit line-of-sight column density is $\log(N_{\text{H,l.o.s}}) = 23.97_{-0.05}^{+0.03}$ and the best-fit average torus column density is $\log(N_{\text{H,tor}}) = 24.16_{-0.10}^{+0.31}$. The best-fit inclination angle is $\cos(\theta_{\text{inc}}) = 0.65_{-u}^{+u}$, suggesting that the inclination angle of Mrk 1066 is fully unconstrained with current data. The best-fit covering factor is $c_{\text{f,tor}} > 0.64$.

NGC 3227: the source is found to be an unobscured AGN with $N_{\text{H,l.o.s}} < 10^{22}$ cm $^{-2}$. We found that the scattering component contribute marginally to the spectrum and abandon of this component does not worsen the fit. Therefore, we set the fraction of the scattering component to be $f_s = 0$ to decrease the free parameters in fitting. The spectra below 1 keV has no obvious emission signature and is hard to be well fitted by **mekal**. We add an phenomenological gaussian and an unabsorbed cut-off power law with a different photon index to fit the soft X-ray spectrum of NGC 3227. The center of the gaussian is at $E_l = 0.62$ keV and the width is $\sigma = 0.05$ keV. The photon index of this phenomenological cut-off power law is measured as $\Gamma_{\text{soft}} = 3.9_{-0.1}^{+0.1}$ compared to the best-fit photon index of the intrinsic cut-off power-law is $\Gamma = 1.68_{-0.01}^{+0.01}$. The best-fit statistic of NGC 3227 is $\chi^2/\text{d.o.f} = 4684/4008 \approx 1.17$. The best-fit line-of-sight column density is $\log(N_{\text{H,l.o.s}}) = 21.39_{-0.01}^{+0.03}$ and the best-fit average torus column density is $\log(N_{\text{H,tor}}) = 23.14_{-0.02}^{+0.03}$. The

best-fit inclination angle is $\cos(\theta_{\text{inc}}) < 0.29$ and the best-fit covering factor is $c_{f,\text{tor}} > 0.93$.

NGC 3783: *NuSTAR* data above 70 keV are polluted by background and the data <10 keV show strong discrepancy with XMM-*Newton*, so we fit the *NuSTAR* spectrum only between 10–70 keV following the approach adopted in previous works (Mehdipour et al. 2017; Mao et al. 2019; De Marco et al. 2020). The cut-off energy E_{cut} of NGC 3783 is found to be $E_{\text{cut}} = 37^{+2}_{-4}$ keV. In addition, we added a number of unresolved Gaussian lines as needed to reach a good fit of Mrk 3783. The best-fit statistic of NGC 3783 is $\chi^2/\text{d.o.f} = 3349/2929 \approx 1.14$. The best-fit photon index is $\Gamma = 1.51^{+0.02}_{-0.04}$. The best-fit line-of-sight column density is $\log(N_{\text{H},\text{l.o.s}}) = 22.85^{+0.01}_{-0.01}$ and the best-fit average torus column density is $\log(N_{\text{H},\text{tor}}) = 25.00^{+0.11}_{-0.22}$. The best-fit inclination angle is $\cos(\theta_{\text{inc}}) = 0.54^{+0.02}_{-0.02}$ and the best-fit covering factor is $c_{f,\text{tor}} = 0.41^{+0.08}_{-0.04}$.

NGC 4051: the source is known to exhibit strong spectra and flux variation in X-ray (Turner et al. 2017). Variability is also found between the *NuSTAR* and XMM-*Newton* observations that we analyzed. The 2–10 keV flux of the *NuSTAR* observation is $\sim 24\%$ less than the XMM-*Newton* observation. This flux variability is caused by the variability of the intrinsic emission rather than the $N_{\text{H},\text{l.o.s}}$ variability based our analysis. The source is also known to possess a warm absorber outflow (Mizumoto & Ebisawa 2016), due to its absorption signature, especially the O VIII absorption feature ~ 0.65 keV, which is difficult to be fitted by the default *mekal* model. We tried to use a complex phenomenological model to fit the spectrum below 1 keV and found that the best-fit results of the key parameters did not vary compared with those obtained when we fitted the spectra only above 1 keV. Therefore, we fit the spectra of NGC 4051 with energy only above 1 keV. The cut-off energy E_{cut} of NGC 4051 is found to be $E_{\text{cut}} = 44^{+2}_{-2}$ keV. The best-fit statistic of NGC 4051 is $\chi^2/\text{d.o.f} = 2686/2389 \approx 1.12$. The best-fit photon index is $\Gamma = 1.72^{+0.01}_{-0.01}$. The best-fit line-of-sight column density is $\log(N_{\text{H},\text{l.o.s}}) = 22.53^{+0.01}_{-0.01}$ and the best-fit average torus column density is $\log(N_{\text{H},\text{tor}}) = 24.45^{+0.07}_{-0.09}$. The best-fit inclination angle is $\cos(\theta_{\text{inc}}) > 0.94$ and the best-fit covering factor is $c_{f,\text{tor}} = 0.95^{+0.01}_{-0.01}$.

NGC 4151: the source is known to exhibit spectral and flux variability in X-ray (Beuchert et al. 2017). Strong variability was also found between the *NuSTAR* and XMM-*Newton* observations in our analysis. The 2–10 keV flux of the *NuSTAR* observation is $\sim 103\%$ larger than the XMM-*Newton* observation. This flux variability is caused by both the variability of the intrinsic emission and the $N_{\text{H},\text{l.o.s}}$ variability based on our analysis. The intrinsic emission measured using *NuSTAR* observation is $\sim 80\%$ larger than the intrinsic emission measured using XMM-*Newton* observation. The line-of-sight column density of the two observations are $\log(N_{\text{H},\text{l.o.s},\text{NuS}}) = 22.86^{+0.02}_{-0.01}$ and $\log(N_{\text{H},\text{l.o.s},\text{XMM}}) = 23.00^{+0.01}_{-0.01}$, respectively. The cut-off energy E_{cut} of NGC 4151 is found to be $E_{\text{cut}} = 112^{+10}_{-16}$ keV. The relative iron abundance is found to be $A_{\text{Fe}} = 0.66^{+0.05}_{-0.05} A_{\text{Fe},\odot}$ when the inclination is fixed at [OIII] measured value in fitting. In addition, we added a number of unresolved Gaussian lines as needed to reach a good fit of NGC 4151. The best-fit statistic of NGC 4151 is $\chi^2/\text{d.o.f} = 5200/4664 \approx 1.11$. The best-fit photon index of NGC 4151 is $\Gamma = 1.67^{+0.02}_{-0.04}$. The best-fit average torus column density is $\log(N_{\text{H},\text{tor}}) = 23.94^{+0.02}_{-0.02}$. The best-fit inclination angle is $\cos(\theta_{\text{inc}}) < 0.08$ and the best-fit covering factor is $c_{f,\text{tor}} = 0.80^{+0.04}_{-0.07}$.

NGC 4507: the source is known to exhibit spectral and flux variability in X-ray (Braitto et al. 2012; Marinucci et al. 2013). Variability was also found between the *NuSTAR* and XMM-*Newton* observations in our analysis. The 2–10 keV flux of the *NuSTAR* observation is $\sim 51\%$ larger than the XMM-*Newton* observation. This flux variability is caused by the variability of the intrinsic emission rather than the $N_{\text{H},\text{l.o.s}}$ variability based on our analysis. The intrinsic emission measured using *NuSTAR* observation is 50% larger than the intrinsic emission measured using XMM-*Newton* observation. The spectrum below 1 keV is difficult to model with a single *mekal*, so we add another *mekal* in fitting the spectrum. The relative iron abundance is found to be $A_{\text{Fe}} = 0.5^{+0.1}_{-0.1} A_{\text{Fe},\odot}$. In addition, we added a number of unresolved Gaussian lines as needed to reach a good fit of NGC 4507. The best-fit statistic of NGC 4507 is $\chi^2/\text{d.o.f} = 1601/1614 \approx 0.99$. The best-fit photon index is $\Gamma = 1.71^{+0.05}_{-0.03}$. The best-fit line-of-sight column density is $\log(N_{\text{H},\text{l.o.s}}) = 23.98^{+0.03}_{-0.05}$ and the best-fit average torus column density is $\log(N_{\text{H},\text{tor}}) = 23.40^{+0.09}_{-0.09}$. The best-fit inclination angle is $\cos(\theta_{\text{inc}}) = 0.43^{+0.10}_{-0.13}$ and the best-fit covering factor is $c_{f,\text{tor}} = 0.55^{+0.09}_{-0.06}$.

NGC 5506: the source is known to exhibit spectral and flux variability in X-ray (Sun et al. 2018). Variability was also found between the *NuSTAR* and XMM-*Newton* observations that we adopted. The 2–10 keV flux of the *NuSTAR* observation is $\sim 18\%$ less than the XMM-*Newton* observation. This flux variability is caused by both the variability of the intrinsic emission and the $N_{\text{H},\text{l.o.s}}$ variability based on our analysis. The intrinsic emission measured using *NuSTAR* is 25% less than the intrinsic emission measured using XMM-*Newton* observation and the line-of-sight column density measured in two observations are $\log(N_{\text{H},\text{l.o.s},\text{NuS}}) = 22.29^{+0.03}_{-0.02}$ and $\log(N_{\text{H},\text{l.o.s},\text{XMM}}) = 22.50^{+0.01}_{-0.01}$, respectively. The relative iron abundance is found to be $A_{\text{Fe}} = 5.8^{+0.4}_{-0.2} A_{\text{Fe},\odot}$. The cut-off energy E_{cut} of NGC 5506 is found to be $E_{\text{cut}} < 21$ keV. In addition, we found that the fit was significant improved (from $\chi^2/\text{d.o.f} = 5590/4544$ to $\chi^2/\text{d.o.f} = 5378/4543$) if we let the photon index of the scattering component free to vary from the one of the intrinsic emission. We measured the photon index of the scattering component as $\Gamma_{\text{soft}} = 1.02^{+0.30}_{-0.02}$ and the best-fit photon index of intrinsic emission is $\Gamma = 1.72^{+0.01}_{-0.01}$. The best-fit statistic of NGC 5506 is $\chi^2/\text{d.o.f} = 5378/4543 \approx 1.18$. The best-fit average torus column density is $\log(N_{\text{H},\text{tor}}) = 23.91^{+0.02}_{-0.02}$. The best-fit inclination angle is $\cos(\theta_{\text{inc}}) = 0.55^{+0.09}_{-0.25}$ and the best-fit covering factor is $c_{f,\text{tor}} > 0.98$.

NGC 5643: a strong emission line at ~ 1.836 keV, which belongs to the Si K β emission line is found. Therefore, a

gaussian line with zero width is added to better fit the spectrum. The best-fit statistic of NGC 5643 is $\chi^2/\text{d.o.f} = 198/170 \approx 1.16$. The best-fit photon index of NGC 5643 is $\Gamma = 1.77_{-0.37}^{+0.27}$. The best-fit line-of-sight column density is $\log(N_{\text{H,l.o.s}}) > 24.33$ and the best-fit average torus column density is $\log(N_{\text{H,tor}}) = 24.15_{-0.35}^{+0.22}$. The best-fit inclination angle is $\cos(\theta_{\text{inc}}) > 0.27$ and the best-fit covering factor is $c_{\text{f,tor}} = 0.50_{-0.23}^{+0.38}$.

NGC 7674: the source is known to exhibit spectra and flux variation in X-ray (Gandhi et al. 2017). Variability was also found between the *NuSTAR* and *XMM-Newton* observations that we adopted. The 2–10 keV flux of the *NuSTAR* observation is $\sim 29\%$ larger than the *XMM-Newton* observation. This flux variability is caused by both the variability of the intrinsic emission and the $N_{\text{H,l.o.s}}$ variability according to our analysis. The intrinsic emission measured using *NuSTAR* observation is 113% larger than the intrinsic emission measured using *XMM-Newton* observation and the line-of-sight column density measured in two observations are $\log(N_{\text{H,l.o.s,NuS}}) = 24.45_{-0.02}^{+0.05}$ and $\log(N_{\text{H,l.o.s,XMM}}) = 24.15_{-0.05}^{+0.08}$, respectively. The relative iron abundance is found to be $A_{\text{Fe}} = 0.42_{-0.08}^{+0.09} A_{\text{Fe},\odot}$. The best-fit statistic of NGC 7674 is $\chi^2/\text{d.o.f} = 240/251 \approx 0.96$. The best-fit photon index is $\Gamma = 2.21_{-0.18}^{+0.12}$. The best-fit average torus column density is $\log(N_{\text{H,tor}}) = 23.65_{-0.05}^{+0.14}$. The best-fit inclination angle is $\cos(\theta_{\text{inc}}) = 0.25_{-0.04}^{+0.52}$ and the best-fit covering factor is $c_{\text{f,tor}} < 0.25$.

Spectra of 13 Sources

Unfolded *NuSTAR*, *XMM-Newton* and *Chandra* spectra of different sources fitted with *borus02* model when the inclination angle is left free to vary and the residuals between the data and best-fit predictions of the model are plotted in Fig. 9 and Fig. 10. The *NuSTAR* data are plotted in blue, the *XMM-Newton* data are plotted in red and the *Chandra* data are plotted in green. The best-fit model prediction is plotted as cyan solid lines. The single components of the model are plotted in black with different line styles, i.e., the absorbed intrinsic continuum with solid lines, the reflection component and Fe $K\alpha$ line with dashed lines, the scattered component, the *mekal* component and gaussian lines with dotted lines.

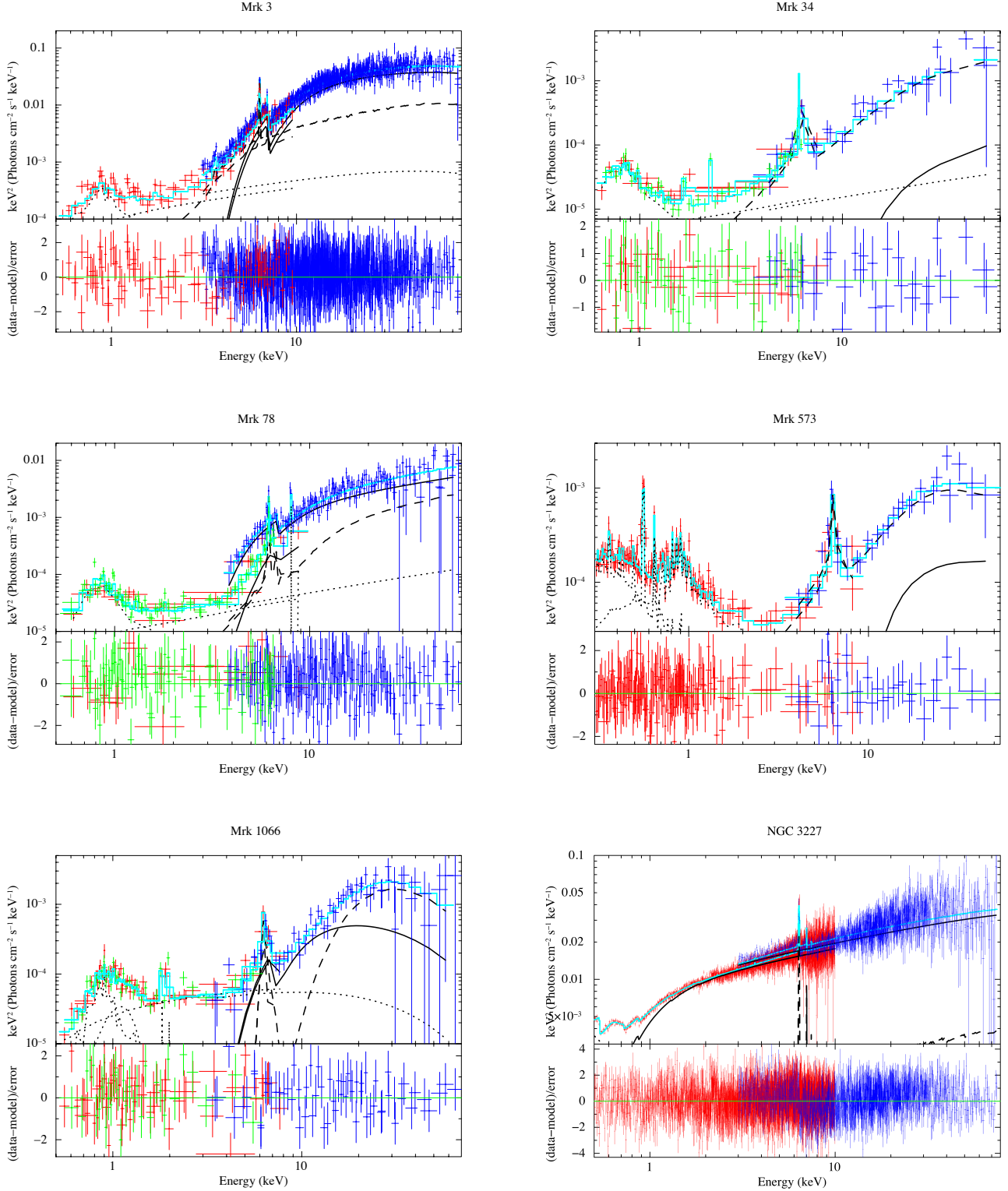


Figure 9. Unfolded *NuSTAR*, *XMM-Newton* and *Chandra* spectra of different sources fitted with `borus02` model when the inclination angle is left free to vary and the residuals between the data and best-fit predictions of the model. The *NuSTAR* data are plotted in blue, the *XMM-Newton* data are plotted in red and the *Chandra* data are plotted in green. The best-fit model prediction is plotted as cyan solid lines. The single components of the model are plotted in black with different line styles, i.e., the absorbed intrinsic continuum with solid lines, the reflection component with dashed lines, the scattered component, the `mekal` component and emission lines with dotted lines.

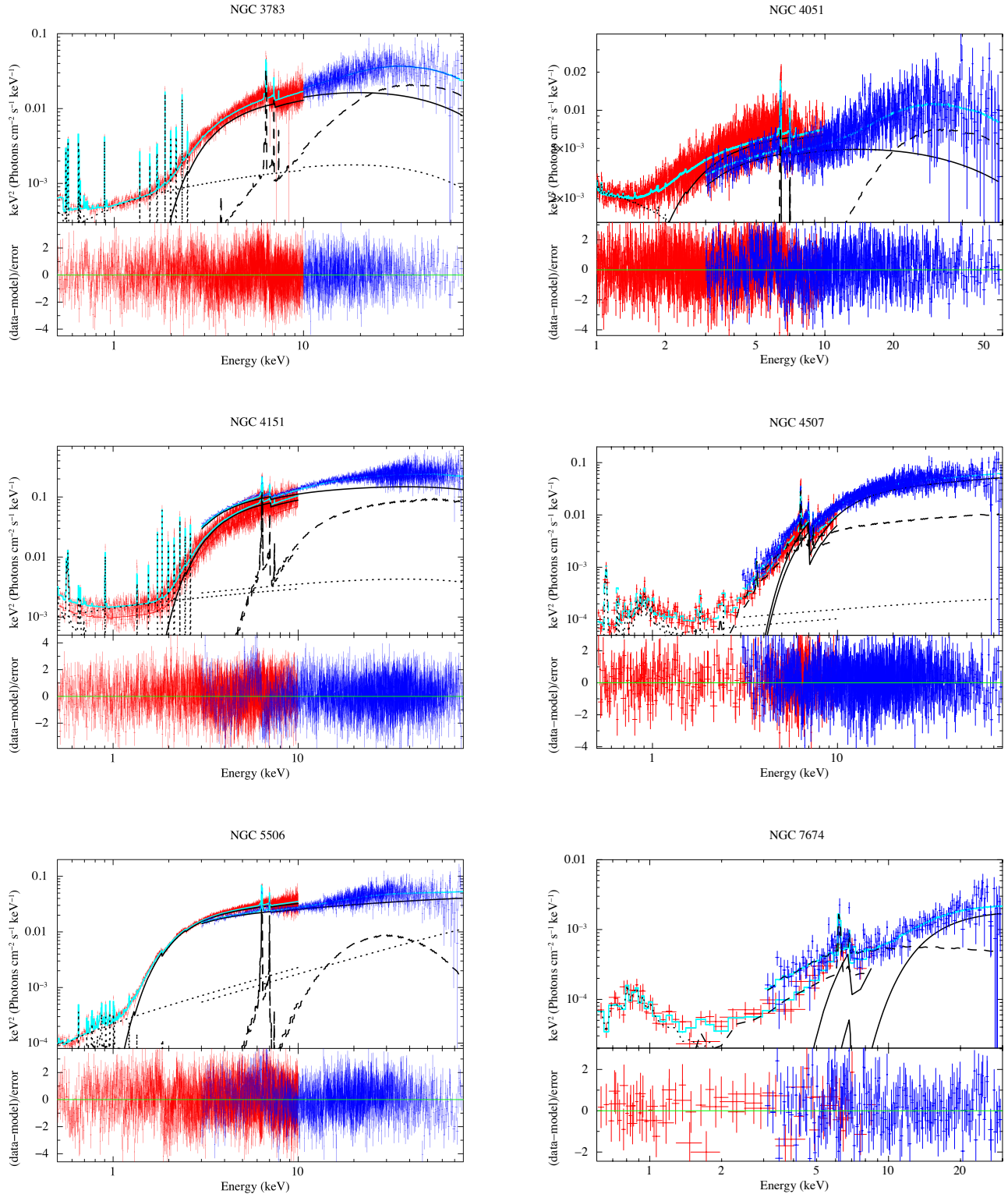


Figure 10. Unfolded *NuSTAR*, *XMM-Newton* and *Chandra* spectra of different sources fitted with *borus02* model when the inclination angle is left free to vary and the residuals between the data and best-fit predictions of the model. The *NuSTAR* data are plotted in blue, the *XMM-Newton* data are plotted in red and the *Chandra* data are plotted in green. The best-fit model prediction is plotted as cyan solid lines. The single components of the model are plotted in black with different line styles, i.e., the absorbed intrinsic continuum with solid lines, the reflection component with dashed lines, the scattered component, the *mekal* component and emission lines with dotted lines.